Published in: IEEE Open Journal of the Communications Society, May 2025. DOI: 10.1109/OJCOMS.2025.3572723

Received Mar. 3, 2025; revised May 2, 2025; accepted May 20, 2025; Date of publication May 22, 2025;
date of current version May 20, 2025.

Digital Object Identifier 10.1109/OJCOMS.2025.3572723

Field Performance Evaluation of a Mechatronic Reflector System in a Private mmWave Network Environment

SIMON HÄGER, MARCEL KAUDEWITZ, FLORIAN SCHMICKMANN, STEFAN BÖCKER, AND CHRISTIAN WIETFELD

Communication Networks Institute (CNI), TU Dortmund University, 44227 Dortmund, NRW, Germany

Corresponing author: Simon Häger (e-mail: simon.haeger@tu-dortmund.de)

This work has been supported by the German Federal Ministry of Education and Research (BMBF) in the course of the *6GEM Research Hub* under the grant number 16KISK038.

ABSTRACT 6G millimeter-wave (mmWave) networks are expected to provide widespread multi-Gbit/s connectivity. However, increased sensitivity to obstacle blockage leads to underconnected shadow regions, motivating the introduction of intelligent reflecting surfaces (IRSs) for efficient smart radio environments that are dynamically illuminated by anomalous reflections. Against this background, this article first presents a comprehensive analysis of the current state of IRS implementations and experimentation. We observe a scarcity of large-scale reconfigurable mmWave IRSs and insufficient experimental insights using communications equipment outside laboratory conditions. To address this gap, we develop *R-HELIOS*, a mechatronically reconfigurable IRS based on our geometry-based passive *HELIOS* IRS, which has previously been validated as a large static IRS in field studies with mmWave modems. It is complemented by a remote-control operation center that systematically orchestrates reflection behavior. The IRS research platform is then integrated into a private mmWave network environment utilizing commercial user equipment (UEs) for 6G-relevant experimentation. In an indoor factory-like scenario, we investigate an IRS beam search mechanism to improve connectivity for shadowed UEs in safety cages for machinery. Serving both UEs with a multi-armed reflection configuration maximizes the cell throughput to 2.1 Gbit/s, constituting an increase by 173 %. In a larger-scale indoor-to-outdoor setup covering an approximately 30 m^2 shadowed study area, the IRS facilitates a mean downlink throughput improvement of 0.9 Gbit/s. Our study thus underscores the high potential of mmWave IRSs for static UEs. Additional measurements with a mobile user highlight the necessity for fine-grained angular beam tracking to mitigate fades at intermediate positions.

INDEX TERMS IRS, mechanical reconfiguration, mmWave communications, 6G networks, field measurements, NLOS, beam management, mobile user, multi-armed beams.

I. TOWARD LARGE RECONFIGURABLE REFLECTORS FOR UBIQUITOUS MMWAVE NETWORK CONNECTIVITY

FUTURE mobile radio networks, such as 6G, are expected to liberally expand to the millimeter-wave (mmWave) and sub-THz domains to offload the limited sub-6 GHz spectrum in hotspot regions [1]. Although the mmWave spectrum currently has many wide bands available, it has been considered a hostile radio environment for wireless communications owing to increased propagation losses. However, a paradigm shift occurred in the last decade [2] which led to the standardization of 5G New Radio (NR) with support for operation in frequency range 2 (FR2) bands containing mmWave frequencies between 24.25 GHz and 71.0 GHz [3, Ch. 3], [4]. In this spectrum, the increased free-space path loss can be compensated for by introducing large-scale antenna arrays and beamforming transceivers.

The associate editor coordinating the review of this manuscript and approving it for publication was Yong Zhou.

mmWave networks may therefore serve user equipment (UEs) in line-of-sight (LOS) conditions at distances of up to approximately 10 km, as recent trials have shown [5, 6]. The typical outdoor coverage range is up to a few hundred meters [7–10]. However, on the downside, reduced obstacle penetration, increased absorption, and reduced diffraction nonetheless reduce the effective cell area of mmWave base stations (BSs) compared to traditional sub-6 GHz cells [7]. Consequently, there are numerous non-line-of-sight (NLOS) regions, particularly in urban areas or indoor factory networks, with poor or no connectivity [11–13]. However, it would be too expensive and energy-consuming to develop them with additional BS sites [14, 15].

To realize efficient ubiquitous mmWave connectivity with future 6G networks, intelligent reflecting surface (IRS) technology has emerged as a candidate solution to the above problem [16–22]. The concept foresees the deployment of reflecting surfaces that intelligently tailor the radio environment in the desired service area of the BS according to the current needs of the network operator. For example, the communications performance can be improved by respectively increasing the received power level and the channel rank, or by suppressing interference. This idea may therefore be summarized by the term smart radio environment (SRE). It has become a hot topic in wireless communications research [16], with contributions from academics and industry covering topics ranging from theory to implementation.

Emerging product prototypes in research and industry are typically semi-passive (i.e., non-amplifying) reflecting surfaces designed for use in the sub-6 GHz spectrum [23, 24]. The reasons for selecting this frequency range include faster time to market and simpler implementation [25]. The synthetic architecture of an IRS ideally allows for *(i)* real-time reconfigurable reflection behavior, i.e., a beamformed reflection towards specific UEs. Moreover, envisioned as *(ii)* large-scale reflecting surfaces, the artificially introduced reflection path of the IRS may enable higher-order communication services. However, in contradiction to the two IRS technology goals *(i)–(ii)*, prototypes available for use in mmWave bands are typically static (i.e., non-reconfigurable) and small. *(iii)* Additionally, mmWave IRS performance is mostly studied under laboratory conditions, with limited transferability of the results to real network deployment scenarios. Consequently, experimental validation of the potential of IRS in real mmWave network environments is scarce and insufficient [26, 27]. This is despite numerous connectivity studies with off-the-shelf cellular mmWave equipment that have emerged in the last few months, either using public [8, 9, 28, 29] or private [13, 30, 31] networks. Summarizing our insights from *(i)–(iii)* in Fig. 1 (cf. survey in Sec. II-B), we identify the lack of a large, reconfigurable mmWave IRS as an open experimental platform facilitating in-field validation of current 6G-related research topics (cf. end of Sec. II-A) as the motivation for this manuscript.

For the above reasons, this study first develops a large

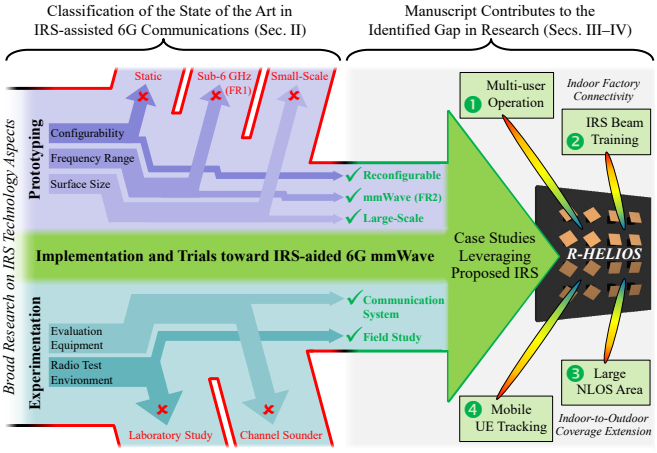

FIGURE 1. Addressing a gap in state-of-the-art 6G research, this article introduces a large reconfigurable mmWave IRS research platform to study connectivity gains and beam management mechanisms with off-the-shelf private cellular network equipment.

and reconfigurable mmWave IRS as follows: Because prior works have already shown that geometry-based reflecting surfaces that mimic synthetic anomalous IRSs can be manufactured at scale and thereby attain high reflection gains that are needed for large-area deployments, we adopt this approach [13, 16]. Moreover, mechatronic components have been leveraged within mmWave and sub-THz reflect-arrays positioned in the vicinity of the antenna, such that flexible transceivers for directional communications are attained at a low cost. We combine the two concepts in our 6G research prototype and assess its performance in terms of loss and power consumption. In the second part of this article, we integrate the remote-controllable IRS in our mmWave network. We study the impact on physical to application layer parameters in downlink (DL) and uplink (UL) directions considering static or mobile and one to multiple active UEs. This is to fill the previously identified gaps in experimental insight of mmWave IRS in-field performance, yielding valuable insights for the realization of future 6G IRS deployments as well as corresponding monitoring and control functions on the network side.

Against this background, the three key contributions of this article are summarized below.

- We present a comprehensive analysis of the current state of experimental validation of IRSs, which serves as the primary motivation for our prototyping and experimentation in this article. To the best of our knowledge, this overview is unique in both scope and depth.
- A geometry-based reconfigurable IRS prototype is implemented leveraging 3D-printed surfaces and servomotors. It can be remotely controlled in real time using a robust sub-6 GHz link. After calibration, we investigate its performance metrics such as the reflection gain, power consumption, and misalignment loss. (Available via [32].)
- The IRS is transferred into two measurement setups with a state-of-the-art mmWave network and UEs. We explore

the wireless communication performance in the context of several aspects of high importance for 6G, such as IRS multi-user communications, support of mobile users, and large-scale coverage in NLOS service areas.

The remainder of this manuscript is structured as follows. Sec. II provides a detailed background on IRS technology, with a focus on existing prototypes and their experimental validation. Then, we present our mechatronically reconfigurable mmWave IRS in Sec. III. Sec. IV evaluates its impact in two different deployment scenarios to assess the performance in the scope of sample use cases of high interest for 6G research and standardization. Finally, Sec. V summarizes the key results of this work and provides a brief outlook on our future works.

II. STATE OF THE ART IN IRS TECHNOLOGY

This section provides an overview of IRS technology. First, we discuss the broad technology concept in Sec. II-A and elaborate on challenges to be addressed for future 6G. Subsequently, Sec. II-B contributes a survey on existing IRS prototypes and experimentation. This underlines our previous motivation for the contributions of this article being the implementation of a mechanical IRS in Sec. III and the experimental case studies conducted in Sec. IV using a real mmWave communication system.

A. Preliminary: IRS-aided Communications toward 6G

Since about 2018, IRSs have rapidly emerged as a transformative, mainstream technology concept for future wireless communication networks, promising improved coverage, enhanced spectral and energy efficiency, and reduced costs [33, 34]. It typically consists of a large uniform $M \times N$ array (M rows, N columns) of synthetic reflecting elements, so-called unit cells with width a and height b, each capable of independently adjusting the phase, amplitude, or polarization of incoming electromagnetic (EM) waves in a frequency-selective manner. Through intelligent control of all $M \cdot N$ elements, an IRS can reconfigure the wireless propagation environment, creating favorable radio conditions for communications. In the scope of future 6G networks, SRE use cases extend beyond traditional communication services, for example, IRSs are also envisioned to assist positioning and sensing services, wireless power transfer, or enhancing communication secrecy [16–18, 34].

At this point, we note that there are various synonyms for IRSs in the literature. For example, a reconfigurable intelligent surface (RIS) emphasizes the real-time reconfigurability of each unit cell (m, n), a large intelligent surface (LIS) highlights the size $(M \cdot b) \times (N \cdot a)$ of the surface, a frequency-sensitive surface (FSS) underlines design frequency and bandwidth aspects, and a software-controlled metasurface (SCM) focuses on remote control functionality [18, 35]. Moreover, the terms engineered electromagnetic surface (EES) and EM skin emphasize custom-tailored IRSs with low thickness [36, 37].

In the following paragraphs, we first introduce the technical terms that are leveraged in this work to characterize IRS prototypes. We further define what a large reflecting surface is and discuss the key advantage of deploying them. Finally, timely IRS research topics to which this article contributes experimentally are outlined.

Feature-dependent Terminology for IRSs

In this work, we focus on *reflecting* IRSs that can be mounted on building walls or similar infrastructure. However, we note that there are also *transmit* IRSs for improved outdoor-to-indoor connectivity, and vice versa. They are ideally transparent and deployed at building or vehicle windows for better penetration. Both features can be combined to realize a simultaneously transmitting and reflecting (STAR) IRS [35].

However, the general idea is the same: The IRS facilitates an anomalous reflection or transmission for the incident EM wave, contrary to the one expected for common building materials (e.g., walls or windows). A *synthetic* IRS realizes this according to the generalized law of reflection [38], e.g., by using patch antenna elements with predetermined dimensions that actively induce a phase change in the EM wave or instead via passive dipoles with predetermined size and rotation angle [23]. The unit cells in the scope of this concept are typically smaller than the wavelength λ and tailored to the targeted spectrum band [16–18, 25]. Alternatively, *geometry-based* IRSs leverage Snell's natural law of reflection and are shaped accordingly. In this case, the leveraged geometries are typically much larger than λ [16, 39, 40].

An IRS is *reconfigurable* if the reflection can be altered electronically or mechanically in real time after deployment [16–18, 25]. The reconfiguration time when switching between beam codebook entries depends strongly on the implementation approach from few ns to about 100 ms [23, 24]. Alternatively, an IRS can be deemed *static* if it exhibits fixed reflection characteristics. Therefore, it must be intelligently preconfigured for the foreseen deployment scenario [41].

The reflection of the IRS can be arbitrarily customized to realize the desired SRE conditions, either on-demand or in advance. Typically, it is either *beamformed* in a certain direction or *broadcasted* to serve a larger area [42]. Alternatively, *multi-armed beams* can be employed to efficiently serve distributed UEs whereas in some use cases nulls are enforced in certain directions of the reflection pattern to reduce interference [43–47].

An IRS is typically a *semi-passive* device that requires power for the control circuitry and to operate a control link to the wireless network. Moreover, some IRSs integrate sensor systems for channel estimation [48, 49]. Depending on the realization approach, a small but continuous power supply may be required for the unit cells to maintain their current configurations [24, 50]. Hence, self-sufficient deployments could integrate an energy storage and photovoltaic modules [51]. *Entirely passive* IRS realizations are feasible for static IRSs [36, 37, 39, 52]. In contrast, *active* IRSs

include hardware for signal amplification, thereby yielding similarities with competing technology concepts, namely, repeaters and relays [39, 53].

Why do we need large IRSs for 6G?

IRSs exhibit a high reflection gain σ, also known as the bistatic radar cross section (RCS) with unit m^2, in the desired direction in terms of azimuth and elevation angles ϕ and θ. According to the radar equation, the received power level P_{RX} at the receiver is directly proportional to σ:

$$P_{\mathrm{RX}} = \frac{P_{\mathrm{TX}} \cdot G_{\mathrm{BS}} \cdot G_{\mathrm{UE}} \cdot \sigma_{\mathrm{IRS}} \cdot \lambda^2}{(4\pi)^3 \cdot d_{\mathrm{BS,IRS}}^2 \cdot d_{\mathrm{IRS,UE}}^2} \tag{1}$$

with transmit power P_{TX}, respective antenna gains G, and distances d from IRS to BS and UE. Hence, maximization of the RCS is crucial. This is easily attained by implementing large IRSs because they are dependent on the reflecting surface area squared, i.e., $\sigma \propto (N \cdot a \cdot M \cdot b)^2$ [42, 54].

The reflecting surface is considered large if its height and width are in the order of 10 to 100 wavelengths [42, 55]. For example, 16λ is assumed in [56, 57]. This would result in multi-meter apertures at traditional sub-6 GHz frequencies, such that much smaller surfaces are already deemed large in practice, e.g., with 0.5 m side lengths [58, 59]. The definition depends somewhat on the considered deployment scenario, for example, 0.2 m to 1.0 m can be considered sufficiently large in an indoor scenario [60]. Because of the short wavelengths at mmWave frequencies, IRSs designed for use in the FR2 spectrum are deemed to be large-scale with much smaller dimensions than those in the frequency range 1 (FR1) band. A size of 0.57 m ($\ll 100\lambda$) was identified as sufficiently large to provide LOS-equivalent connectivity within a 28 GHz outdoor campus deployment in [61] using analytic methods. At the same frequency, the authors in [62] deem 0.2 m (ca. 20λ) as too small. To combine these above considerations, this work considers IRSs as large when having dimensions of at least 1.0 m at low frequencies, i.e., $\geq 10\lambda$ at 7.125 GHz being the border between 3GPP FR1 and frequency range 3 (FR3) spectrum [4, 63]. We consider an mmWave IRS large when exhibiting at least 0.3 m side lengths. This is approximately 25λ at 24.25 GHz, which marks the beginning of the 3GPP high-band spectrum, specifically FR2 [3, Ch. 3].

Research Topics for IRS-aided 6G mmWave Networking

Various research challenges need to be addressed toward IRS-enabled beyond line-of-sight (BLOS) mmWave communications. In the following paragraphs, we discuss the ones to which our experimental results from Sec. IV contribute.

Characterization of System-level Performance: Some research and industry activities focus on evaluating mmWave IRSs individually under laboratory conditions. In this scope, received power measurements, depending on the frequency and angles of incidence and departure, are conducted at short distances [64–69]. However, these results cannot be directly transferred to real-world communication system settings. The performance depends on further factors, such as the deployment scenario, transceiver hardware, and communication system mechanisms. Therefore, meaningful studies with communication equipment have to make direct comparisons between the power levels with and without IRS. Some research papers also extend this comparison to the gains in the application data rate. Contemporary literature often studies the attainable received power gain which can be compared with laboratory measurements. Peak performance estimates are usually reported by placing the receiver in an artificially created deep shadow region, or alternatively, no LOS blockage is required if a highly directional single-input single-output (SISO) system is employed [55, 70–74]. *In contrast to these studies, we employ an mmWave system capable of using two multiple-input multiple-output (MIMO) layers, cf. Sec. IV-A, thereby allowing for more profound insights leveraging the channel rank metric. Moreover, by considering all three parameters in a scenario similar to that of private industry networks, we report the regular system performance gains.* Our contribution is therefore important for future decision-making in the scope of 6G network planning, i.e., whether to use additional BSs, network-controlled repeaters (NCRs), or IRSs [39, 53, 75].

BS–UE Beam Management in the Presence of IRSs: Introduced with 5G networks, beam management is a critical aspect of mmWave communications requiring electronically steerable antenna array gains on the BS and UE sides to compensate for increased propagation losses. There are procedures for link establishment and maintenance, such as beam training, beam tracking, and beam switching [3, Ch. 12], [76]. Many studies have investigated this topic in the last decade, as it is deemed a make-or-break component for the success of mmWave communications in dynamic environments. Outdoor and indoor trials with standardized equipment have confirmed that these mechanisms work reasonably well if small beambooks are employed on either side [8, 13, 30]. Moreover, we recently demonstrated the compatibility of current generation mmWave networks with static IRSs which are seamlessly adopted by the network, even without introducing an IRS-aligned pencil beam in the BS beambook for higher gain [77]. Naturally, this effect can also be observed with a manually tuned beam of a reconfigurable IRS, cf. [44]. In contrast to the above works, the studies [55, 78, 79] presented received power heatmaps by static IRSs over larger areas instead of for a single UE position. In our previous work [80], we similarly considered connectivity along a fixed trajectory and investigated BS-side beam switching selecting between two static IRSs to serve the mobile UE either with low gain over a larger region or with high gain at a specific location. Although there have been studies using sub-6 GHz IRSs to determine a beam sweeping-based peak connectivity level for each position over an area of interest, for example, in [81, 82], to the best of our knowledge, there is none for the mmWave spectrum. *Hence, this work contributes to the state of the art with connectivity radio environmental*

maps (REMs) of received power, rank indicator, beam index, and throughput levels with and without IRS in Sec. IV-C.

IRS-assisted Beam Management: Naturally, there has been a lot of analytical and simulative research on beam management for 6G IRS-assisted communications [18]. However, experimental research on this topic with reconfigurable IRSs is limited with most works focusing on IRS system readiness, e.g., leveraging liquid crystal-based IRSs for fast beam switching with low power consumption [24], integrating the ability of fine-grained azimuth and elevation angle sweeping in [83], provisioning of multi-armed beams to serve multiple UEs simultaneously [43, 84] (and even in different bands in [85]), or improved near-field communications via beamfocusing reflection patterns by angular plus radial beamforming in [86]. Some experimental studies have yielded operational beam management insights in the following research areas:

- *IRS Beam Training* aims to establish the optimal IRS configuration such that a high-quality artificial NLOS propagation path is established. Using $M \cdot N$ control signal measurements (equal to the number of IRS unit cells) between the BS and UE with random IRS configurations, a fast IRS beam training approach is proposed in [87] and tested for a static UE at different distances. A similar concept is evaluated in [88]. By introducing an additional link between the UE and IRS, the number of control signal measurements can be reduced to $M + N$ [26]. However, [26, 87, 88] only experimented with sub-6 GHz equipment. The authors in [89] study horizontal beam sweeping to identify a suitable mmWave IRS configuration for two different IRS positions and selected static UE positions. [90] trials exhaustive and hierarchical approaches over a limited azimuth angle range. *This work similarly contributes to mmWave beam training, however, with extensive joint horizontal and vertical beam sweeping in Sec. IV-B.*
- *IRS Multiple Access* considers how to configure an IRS that serves multiple UEs such that they may connect with the cellular network. It is typically assumed that the respective beam training was successfully achieved. For this purpose, an IRS may switch between states over time, matching the typical RIS concept. Alternatively, the unit cells are configured to exhibit a multi-armed beam [43–46], e.g., by splitting the overall IRS into sub-arrays with different beamforming configurations. Potentially, the IRS can be configured to have frequency-selective reflection beams tailored to narrow bands within its operating bandwidth [85]. The authors in [45] employ a sub-6 GHz IRS to balance the overall throughput between two UEs with different beam configurations serving either one or both UEs. Similarly, [46] balanced the received power levels of two UEs. *This manuscript transfers the above two works to the mmWave spectrum and studies multi-user cell traffic in Sec. IV-B with the IRS switching between serving none of the two UEs, one of them, or both. In this context, a brief sensitivity analysis considers which IRS size would be sufficient by intentional misalignment of the IRS modules.*
- *IRS Beam Tracking* conducts continuous updates of the reflection characteristics to seamlessly serve a mobile user. Ultra-wideband (UWB)-based tracking of a mobile user is demonstrated in [49], whereas a camera vision-based approach is shown in [91]. Both trials were performed in the FR1 spectrum. [90] tests neighbor beams if end-to-end link strength drops below a predefined threshold. The authors in [48] integrated channel-sensing functionality into six (from a total of 100) unit cells of their mmWave IRS prototype. All four studies were within a very short distance of the IRS under laboratory conditions. *Against this background, our work provides insights into mmWave IRS beam tracking at larger distances in Sec. IV-C.*

B. Large Reconfigurable mmWave IRSs: Few Prototypes and Limited Field Trials with Communication Systems

This section builds upon the previously introduced terminology and research topics by reviewing experimental prototypes and trials involving IRSs. First, we outline the methodology employed in our literature review. Following this, we discuss the observed trends that serve as the motivation for this work.

Methodology for Literature Review

Numerous analytical and simulative studies on IRS-aided wireless communications underline the high potential of mmWave IRSs [18]. However, depending on the assumptions and level of detail in the modeling, predictions may strongly deviate from real-world performance [92]. For this reason, experimental trials are crucial for testing, developing, and comparing procedures because it confirms key results under hardware limitations and enables the refinement of models and technologies to meet the demands of future 6G networks.

Tab. 1 gives an overview of validated and demonstrated IRS prototypes along the whole 6G spectrum, sorted from 2.3 GHz in FR1 up to frequencies well in the mmWave spectrum and beyond the FR2 spectrum of interest in this work. The architecture of the IRS is characterized by classifying between static or reconfigurable reflection behavior and synthetic or geometry-based realization of the artificial reflection. We then characterize the conducted measurements: The table differentiates between measurements with *channel sounder* (e.g., VNA or SDR/FPGA-based equipment), primarily used for received power or CIR measurements using different incident and reflect angle combinations and carrier frequencies, or *communication system* (e.g., WLAN/cellular or SDR/FPGA-based) equipment for measurements of the physical channel and link to application layer parameters, such as throughput, received power, SNR, BER, and EVM[1]. Moreover, we distinguish between *laboratory* (e.g., anechoic chamber, office room, tailored scenario) and *field* (e.g., out-

[1] Abbreviations used in sentence: channel impulse response (CIR), vector network analyzer (VNA), software-defined radio (SDR), field-programmable gate array (FPGA), wireless local area network (WLAN), signal to noise ratio (SNR), bit error rate (BER), and error vector magnitude (EVM).

TABLE 1. Literature overview of IRS prototypes that have been experimentally demonstrated. Studies relying solely on analytical methods or EM simulations are excluded. A lack of field studies involving mmWave (FR2) communication systems and large reconfigurable IRSs becomes evident, which is therefore addressed in this article.

References	EM Spectrum: FR1	FR3	FR2	sub-THz	Frequency (GHz)	Architecture: Static	Reconfigurable	Synthetic Cells	Geometry-based	Measurements: Channel Sounder	Commun. Syst.	Laboratory	Field	Form Factor of Prototype: Arrangement	Height × Width (cm)	Large-scale IRS†	Power Demand: Static Beam*	Beam Switching*	Syst. Power (W)	Further Details
Focus on IRSs for FR2 mmWave Communications																				
[93]	●	○	○	○	2.3	○	●	●	○	●	○	●	○	16 × 16	80.0 × 80.0	○	●	●	153.0	
[50]	●	○	○	○	2.4	○	●	●	○	●	○	●	○	1 × 4	5.2 × 23.6	○	●	●	0.12	
[94]	●	○	○	○	2.4	○	●	●	○	●	●	●	●	25 × 128	78.2 × 320.0	◐	●	●	N/A	
[45]	●	○	○	○	2.6	○	●	●	○	○	●	●	○	12 × 12	35.2 × 35.2	○	●	●	N/A	
[82, 95]	●	○	○	○	2.6	○	●	●	○	●	●	○	●	32 × 16	160.0 × 80.0	○	●	●	5.87 - 12.01	
[88]	●	○	○	○	2.6	○	●	●	○	○	●	○	●	16 × 16	200.0 × 200.0	●	●	●	30.0 - 40.0	
[96]	●	○	○	○	3.2	○	●	●	○	●	○	●	○	16 × 16	45.0 × 40.7	○	●	●	N/A	
[97]	●	○	○	○	3.5	○	●	●	○	●	○	●	●	32 × 32	96.0 × 96.0	○	●	●	0.01*	
[51, 98]	●	○	○	○	3.5	○	●	●	○	●	○	○	●	81 × 30	111.6 × 114.0	●	●	●	3.6	Opt.: Solar-powered
[99]	●	○	○	○	3.6	○	●	●	○	○	●	○	●	2 × 24	119.0 × 76.0	◐	●	●	N/A	Active IRS
[42]	●	○	○	○	4.3	○	●	●	○	●	○	●	○	8 × 32	9.6 × 38.4	○	●	●	0.72	
[100]	●	○	○	○	4.4	○	●	○	●	●	○	●	○	8 × 25	40.0 × 50.0	○	●	●	50.0	
[101]	●	○	○	○	2.6, 4.9	○	●	●	○	●	●	○	●	20 × 20 - 32 × 32	100.0 × 100.0	●	●	●	N/A	ZTE
[102]	●	○	○	○	5.2	○	●	◐	○	●	○	●	○	20 × 20	60.0 × 60.0	○	●	●	N/A	Opt.: Geometry feature ①
[103-105]	●	○	○	○	5.2	○	●	●	○	●	●	●	○	10 × 8 - 16 × 20	32.0 × 24.0 - 48.0 × 64.0	○	●	●	N/A	Greenerwave
[106]	●	○	○	○	5.3	○	●	●	○	●	○	●	○	10 × 10	28.3 × 28.3	○	●	●	0.06	NEC
[91]	●	○	○	○	5.4	○	●	●	○	●	○	●	○	20 × 20	28.0 × 28.0	○	●	●	≤0.5	
[49, 107]	●	○	○	○	5.4	○	●	●	○	●	○	●	○	16 × 16 - 48 × 64	32.0 × 40.0 - 74.1 × 144.0	◐	●	●	N/A	
[108]	●	○	○	○	5.5	○	●	●	○	●	○	●	○	4 × 4	25.0 × 22.0	○	●	●	N/A	Opt.: Active IRS
[109]	●	○	○	○	5.5	○	●	◐	●	●	○	●	○	21 × 20	52.5 × 48.0	○	○	●	N/A	Opt.: Synthetic feature ①
[110]	●	○	○	○	5.8	○	●	●	○	●	○	●	○	11 × 11	27.5 × 27.5	○	●	●	N/A	
[46]	●	○	○	○	5.8	○	●	●	○	●	○	●	○	16 × 16	57.9 × 57.9	○	●	●	N/A	
[81]	●	○	○	○	5.8	○	●	●	○	●	○	●	●	10 × 16	25.9 × 41.4	○	●	●	≤0.66	
[87]	●	○	○	○	5.8	○	●	●	○	○	●	●	○	16 × 16	36.2 × 36.2	○	●	●	N/A	
[26]	●	○	○	○	5.8	○	●	●	○	●	●	●	●	20 × 55	20.5 × 78.7	○	●	●	2.43	
[111]	●	○	○	○	6.9	○	●	●	○	○	●	●	●	32 × 32	61.0 × 61.0	○	●	●	N/A	
[112]	●	○	○	○	7.0	○	●	◐	●	●	○	●	○	80 × 80	87.0 × 87.0	○	○	●	N/A	Opt.: Synthetic feature ②
[113]	○	●	○	○	9.5	○	●	◐	●	●	○	●	○	7 × 7	17.7 × 17.7	○	○	●	N/A	Opt.: Synthetic feature ②
[36, 114]	●	●	○	●	5.5, 10.0, 83.5	●	○	●	○	●	○	●	●	15 × 15 - 37 × 37	16.0 × 16.0 - 102.0 × 102.0	●	○	○	0	
[115, 116]	●	●	○	○	5.6, 10.0	○	●	●	○	●	○	●	○	10 × 10	50.0 × 50.0	○	●	●	N/A	
[117]	○	●	○	○	10.0	○	●	●	○	●	○	●	○	10 × 10	10.0 × 10.0	○	●	●	N/A	
[118]	○	●	○	○	10.0	●	○	●	○	●	○	●	○	60 × 60	24.0 × 24.0	○	○	○	0	Transmit IRS
[42]	○	●	○	○	10.5	○	●	●	○	●	○	●	○	50 × 34 - 102 × 100	50.0 × 34.0 - 100.0 × 102.0	●	●	●	≤13.36	
[119, 120]	○	●	○	○	10.0, 10.7	○	●	◐	●	●	○	●	○	12 × 20	15.8 × 17.0	○	○	●	11.25	Opt.: Synthetic feature ②
[121]	○	●	○	○	10.7	○	●	●	○	●	●	●	●	10 × 10	20.8 × 22.8	○	●	●	N/A	
[122]	○	●	○	○	13.5	○	●	●	○	●	○	●	●	16 × 16	16.0 × 16.0	○	●	●	N/A	
[123]	○	●	○	○	18.0	●	○	●	◐	●	○	●	○	30 × 30	15.0 × 15.0	○	○	○	0	Opt.: Geometry feature ①
[70]	○	○	●	○	24.5	○	●	●	○	○	●	●	○	32 × 32	9.6 × 9.6	○	●	●	0.33	
[124, 125]	○	○	●	○	24.5, 26.0	○	●	●	○	●	●	●	○	28 × 76	12.0 × 19.8	○	●	●	N/A	Transmit and reflect IRS
[126]	○	○	●	○	26.0	●	○	◐	●	●	○	●	○	14 × 14	7.0 × 7.0	○	○	○	0	Opt.: Synthetic feature ②
[127]	○	○	●	○	26.0	●	○	○	●	●	○	●	○	49 × 37	81.3 × 61.0	○	○	○	0	
[37, 128]	○	○	●	○	26.0	●	○	●	○	●	○	○	●	100 × 100 - 100 × 150	244.0 × 244.0 - 244.0 × 366.0	●	○	○	0	
[129]	○	○	●	○	26.0	○	●	●	○	●	○	○	●	16 × 16	N/A	○	●	●	N/A	
[130, 131]	○	○	●	○	26.0	○	●	●	○	●	○	●	●	48 × 48	15.3 × 15.3	○	●	●	N/A	
[101, 132]	○	○	●	○	26.0	○	●	●	○	●	●	●	●	64 × 64	29.7 × 42.0	◐	●	●	N/A	ZTE
[133, 134]	○	○	●	○	26.9	○	●	●	○	●	●	●	●	45 × 50	22.5 × 25.0	○	●	●	0.05	
[71]	○	○	●	○	27.0	◐	●	●	○	○	●	●	○	20 × 56	5.6 × 7.8	○	●	●	≤1.36*	Static 20 × 8 sub-array
[72]	○	○	●	○	27.0	○	●	●	○	○	●	●	○	16 × 16	7.9 × 7.9	○	●	●	N/A	Transmit IRS
[44, 89]	○	○	●	○	27.0	○	●	●	○	●	●	●	●	40 × 40	20.0 × 20.0	○	●	●	2.0 - 35.0	Greenerwave
[83]	○	○	●	○	27.2	○	●	●	○	●	○	●	○	16 × 16 - 32 × 32	8.6 × 8.6 - 17.2 × 17.2	○	●	●	N/A	
[64]	○	○	●	○	27.5	○	●	●	○	●	○	●	○	20 × 20	7.7 × 7.7	○	●	●	1.0	
[55]	○	○	●	○	27.9	●	○	●	○	○	●	○	●	N/A	80.0 × 80.0	●	○	○	N/A	NTT Docomo
[135, 136]	○	○	●	○	28.0	●	○	●	○	●	○	●	○	51 × 51	28.0 × 28.0	○	○	○	0	TMYTEK
[137]	○	○	●	○	28.0	●	○	○	●	●	○	●	○	1 × 1	46.0 × 11.0 - 34.0 × 34.0	●	○	○	0	
[52, 78]	○	○	●	○	28.0	●	○	○	●	●	○	○	●	36 × 21 - N/A	20.0 × 10.0 - 42.0 × 52.5	●	○	○	0	Samsung
[79]	○	○	●	○	28.0	●	○	●	○	○	●	○	●	N/A	40.0 × 200.0	●	○	○	0	Transmit IRS
[65]	○	○	●	○	28.0	○	●	●	○	●	○	●	○	24 × 24	8.8 × 8.8	○	●	●	N/A	
[66]	○	○	●	○	28.0	○	●	●	○	●	○	●	○	20 × 20	10.9 × 10.9	○	●	●	N/A	
[138, 139]	○	○	●	○	28.0	○	●	●	○	●	○	●	○	40 × 40	23.0 × 23.0	○	●	●	23.0	TMYTEK
[48]	○	○	●	○	28.0	○	●	●	○	○	●	●	○	10 × 10	5.0 × 5.0	○	●	●	N/A	6 cells reflect and sense
[90]	○	○	●	○	28.0	○	●	○	●	●	○	●	○	20 × 20	10.0 × 10.0	○	●	●	3.9	
[77, 80, 140]	◐	○	●	○	27.1, 28.5	●	○	◐	●	●	○	●	●	4 × 4 - 10 × 5	40.0 × 40.0 - 80.0 × 40.0	●	○	○	0	Opt.: Synthetic feature ③
[141, 142]	○	○	●	○	28.0, 28.5	●	○	●	○	●	○	●	○	25 × 32	10.0 × 16.0	○	●	●	N/A	
[143, 144]	○	○	●	○	28.0, 28.5	○	●	●	○	●	○	●	○	20 × 20	10.0 × 10.0	○	●	●	3.0 - 16.0	
[73, 145]	○	○	●	○	28.5	○	●	●	○	○	●	●	○	16 × 16 - 48 × 48	10.0 × 10.0 - 30.0 × 30.0	●	●	●	N/A	
[67]	○	○	●	○	29.0	○	●	●	○	●	○	●	○	24 × 24	12.0 × 12.0	○	●	●	N/A	Samsung
[146]	○	○	●	○	30.0	○	●	●	○	●	○	●	○	80 × 80	9.6 × 9.6	○	○	○	0	Transmit and reflect IRS
[147]	○	○	●	○	30.0	●	○	○	●	●	○	●	○	52 × 52	15.6 × 15.6	○	○	○	0	
[69]	○	○	●	○	32.0	○	●	◐	●	○	●	●	○	14 × 26	11.2 × 11.2	○	○	●	3.5	Opt.: Synthetic feature ②
[43, 148, 149]	○	○	●	○	35.0	○	●	●	○	●	○	○	●	60 × 60	22.8 × 22.8	○	●	●	15.75 - 103.2	
[150]	○	○	●	○	28.0, 39.0	●	○	●	○	●	○	●	●	N/A	79.0 × 81.0	●	○	○	0	Opt.: Synthetic feature ③
[47, 151]	○	○	●	○	30-40	●	○	○	●	●	○	●	○	1 × 1 / 7-hex	10.0 × 10.0 - 23.6 × 23.6	○	○	○	0	
[86]	○	○	●	○	58.3	○	●	●	○	●	○	●	○	80 × 80	20.0 × 20.0	○	●	●	N/A	Near-field IRS
[152]	○	○	●	○	60.0	●	○	●	○	●	○	●	○	75 × 75	15.0 × 15.0	○	○	○	0	
[68]	○	○	●	○	60.0	○	●	●	○	●	○	●	○	14 × 16	33.7 × 34.5	●	●	●	N/A	
[153]	○	○	●	○	60.3	○	●	●	○	●	○	●	○	160 × 160	57.4 × 57.4	●	●	●	234.0	
[24]	○	○	●	○	61.0	○	●	●	○	●	○	●	○	20 × 6	N/A	○	●	●	18μ*	
[74]	○	○	●	○	64.0	●	○	◐	●	○	○	○	●	64 × 64 - 128 × 128	8.0 × 8.0 - 16.0 × 16.0	○	○	○	0	Opt.: Synthetic feature ①
[84, 85]	○	○	●	●	28-39, 100	●	○	●	○	●	○	●	○	40 × 40 - 45 × 45	6.8 × 6.8 - 20.3 × 20.3	○	○	○	0	
[154]	○	○	●	●	28, 39, 120	●	○	●	○	●	○	●	○	1 × 1	40.6 × 40.6	●	○	○	0	Opt.: Synthetic feature ③
[155-157]	○	●	●	●	11-26, 75-110	●	○	●	○	●	○	●	○	8 × 8 - 21 × 21	1.6 × 1.6 - 35.7 × 35.7	●	○	○	0	
[158]	○	○	○	●	145.5	●	○	○	●	●	○	○	●	1 × 1	N/A	●	○	○	0	
[159]	○	○	○	●	300.0	○	●	○	●	●	○	○	●	1 × 80	2.4 × 0.5	○	○	●	N/A	
This Work	○	○	✓	○	27.1	○	✓	○	●	○	✓	○	✓	4 × 4	66.3 × 67.3	✓	○	●	1.33 - 31.10	

Feature Classification: ● – Yes. ◐ – Optional/Partially. ○ – No/Inapplicable. N/A – Not Available. Highlighting – Focus Criterion. Highlighting – Exclusion Criterion/Research Gap.

Notes: †: Large IRS has side lengths larger than 10λ. Here: ≥0.3 m in FR2/sub-THz and ≥1.0 m in FR1/FR3 spectra. *: Neglecting power for control circuitry and control link.

Details on Optional Features: ①: For improved reflection behavior. ②: For frequency-selective characteristics. ③: For transparency of IRS.

door deployment scenario, indoor factory hall) environments. We further describe the form factor of the prototypes by listing the unit cell arrangement and the IRS side lengths. The latter is used to characterize whether the IRS is electrically large, i.e., larger than 10 wavelengths (cf. Sec. II-A). Additional columns address the power consumption aspects of the prototypes (if available) and provide further details. Overall, the table has a unique scope and features more than 80 IRSs, thus making it the most extensive compendium of IRS prototypes and experiments to this date.

State of the Art in IRS Prototypes and Experimentation

In the following paragraphs, we discuss related works contained in Tab. 1 that adhere to our *five IRS requirements*, which are highlighted in green within the table if fulfilled: *(i) FR2*, *(ii) reconfigurable*, *(iii) communication system*, *(iv) field*, and *(v) large*. This order was determined by counting the number of prototypes in a column with the respective characteristic and sorting in descending order[2].

(i) FR2 IRS: We primarily focus on mmWave IRSs that target the FR2 spectrum. These are highlighted by the gray box in Tab. 1. Most prototypes of them were designed for the 5G bands n257 and n258 in the range of 24.25 GHz to 29.5 GHz, and less for the unlicensed 60 GHz spectrum (5G band n260, also used by mmWave WLAN). Some of the contained reflecting surfaces have also been measured in the anchor (FR1) or neighboring bands (FR3, sub-THz).

(ii) Reconfigurable IRS: Contrasting IRSs from the sub-6 GHz spectrum that are nearly all reconfigurable, more than 40 % of the FR2 prototypes are static, i.e., non-reconfigurable. Hence, most mmWave IRSs surveyed are reconfigurable. We further note that, with a relative frequency of over 20 %, there are more geometry-based IRS prototypes in FR2 than in FR1. This can be attributed to the smaller wavelengths in FR2, such that IRSs do not have to be infeasibly large to shape the incident EM wave as desired.

Tab. 1 outlines that less than half of the FR2 IRSs are evaluated using a *(iii) communication system*, with a few of those also being evaluated with a channel sounder. With most mmWave IRSs being evaluated purely on the physical layer, the assessment of the system-level implications of IRS deployments needs to be improved. Fewer mmWave IRSs are validated in the *(iv) field*, i.e., in large non-artificial scenarios. Instead, they are validated under laboratory conditions, which are typically large anechoic chambers or compact antenna test ranges (CATRs). Therefore, the experimental validation of the expected performance gains in real scenarios needs to be extended. Both points confirm the findings of the authors in [26, 27], which point out that experimental validation of IRSs in real mmWave network environments is scarce.

(v) Large-scale IRS: At the current stage of research, the least number of IRSs can be considered sufficiently large to be called LIS. Moreover, 7 of the 13 large mmWave IRSs have not been validated in the field with communication systems [68, 73, 127, 137, 153–155]. Further, 77 % of the mmWave LISs are only static [37, 52, 55, 77, 79, 127, 137, 150, 154, 155]. Additionally, although we observe that significantly more unit cells have been aggregated in synthetic mmWave IRSs than in sub-6 GHz IRSs, we still have to note that implementation complexity seems to have limited the scaling of the surface side lengths to less than the factor between the respective carrier frequencies. Otherwise, the table would have listed numerous mmWave RISs featuring at least 100×100 unit cells. Considering the previously noted increase in geometry-based IRSs for mmWave and sub-THz frequencies, it seems that non-synthetic LISs are currently a feasible alternative for crucial experimentation toward 6G.

Considering all five aspects *(i)–(v)*, we note that there is not yet a single research article that meets all criteria. Liu *et al.* [101] make significant progress toward this, though the IRS is smaller than required. Using the IRS to illuminate a UE in an outdoor building shadow to enhance connectivity with the public mmWave network, the authors observe a promising mean in-band received power gain of 12 dB. In an indoor study, up to about 30 dB system gain is realized for a UE in a deep shadow area, thus underlining the high potential of the IRS technology. Nonetheless, the presentation of the measurement setup and results is limited and overshadowed by an emphasis on presenting EM simulation outcomes [101]. Other highly relevant works are limited as follows: The three IRSs [124, 125], [133, 134], and [44, 89] are also too small. Despite this limitation, these studies yielded important contributions to the state of the art. For example, [44] confirmed feasible received power gains of up to 22 dB in an indoor train station scenario with a public mmWave network. Correspondingly, the throughput increases by up to 55 %. Importantly, the authors show that the IRS leads to a stable link, meaning that no cell-side beam switches occur and the link power and throughput are stable if the IRS is active [44]. Whereas the prior discussed works used small IRSs, other recent studies are limited otherwise. For example, no field experiments have been conducted using the prototype in [73]. Moreover, our own IRS [13, 39] and the three presented in [55], [79], and [150] are not reconfigurable. Nonetheless, they also confirmed that this is a viable approach, for example, the static reflector in [55] improves mmWave connectivity along an approximately 20 m long road segment of an urban canyon by up to 15 dB in terms of received power level and 500 Mbit/s in terms of DL data rate.

The above study of related research works at the hands of Tab. 1 therefore clearly confirms our motivation presented in Sec. I. *For this reason, this manuscript aims to implement a large-scale RIS and transfer it into a real-world mmWave network deployment with 3GPP-compliant equipment to study the 6G aspects outlined at the end of Sec. II-A.* The implementation of the large mmWave RIS is attained based on our static IRS *Holistic Enlightening of bLackspots with passIve reflectOr moduleS* (HELIOS), which consists of 3D-printed reflecting modules [39]. HELIOS can be customized using a genetic algorithm that leverages a physical optics-based reflection model [54, 140]. Moreover, our prior works have also already confirmed their positive impact on mmWave communication links, e.g., in a real industrial production scenario [13]. This article thus first extends HELIOS by mechatronic components in Sec. III to realize an open IRS platform. A key advantage of our IRS architecture is the low design complexity compared to synthetic mmWave

[2]Hence, implications of Tab. 1 are, e.g., that most proposed IRSs are reconfigurable but few are of large scale. Also, more IRSs have been validated with a communication system than IRS field trials have been conducted.

IRSs, thus allowing for replication by other researchers. We then leverage the proposed reflector system in our field trials in Sec. IV, thus showcasing its suitability to address the lack of mmWave field experiments with IRSs toward 6G.

III. DEVELOPMENT OF IRS RESEARCH PLATFORM

This section describes the implementation of the IRS platform in Sec. III-A. Thereafter, Sec. III-B calibrates the platform, examines performance metrics, and provides insights into optimized module shapes for specific deployments.

A. Design and Operation of Large Mechatronic RIS

In the following paragraphs, we describe the construction of the IRS. Thereafter, a remote-control operation center is introduced for our trials.

R-HELIOS Reflector System

The goal of our implementation is to make our static HELIOS [39] reflector reconfigurable. It is a geometry-based IRS that leverages 3D-printed modules exhibiting a large, arbitrarily tilted surface. They become highly reflective by applying a conductive coating to them. A genetic algorithm employing an analytical reflection model is used to customize the reflection pattern quickly [54, 140]. Our prior experimental works [13, 77, 80, 140] have validated this concept in laboratory and field environments using channel sounder and communication system equipment. Therein, the individual reflectors exhibited a size of up to $40\,\mathrm{cm} \times 40\,\mathrm{cm}$, such that we categorize them as large-scale IRSs. Against this background, the key idea for our

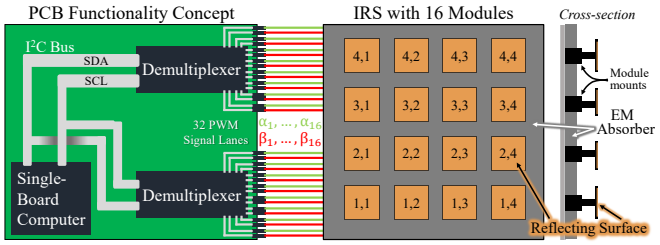

FIGURE 2. **Overall architecture of the mmWave IRS system consisting of 4×4 large reflecting modules. The mechanical tilts are supplied by the SBC.**

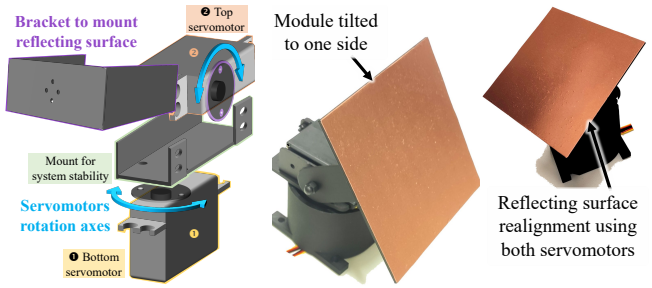

(a) Each module leverages two stacked servomotors. **(b) Assembled module combines architecture from *(a)* with a reflecting surface.**

FIGURE 3. **Employed reconfigurable geometries for modular integration into our Reconfigurable HELIOS (R-HELIOS) IRS research platform.**

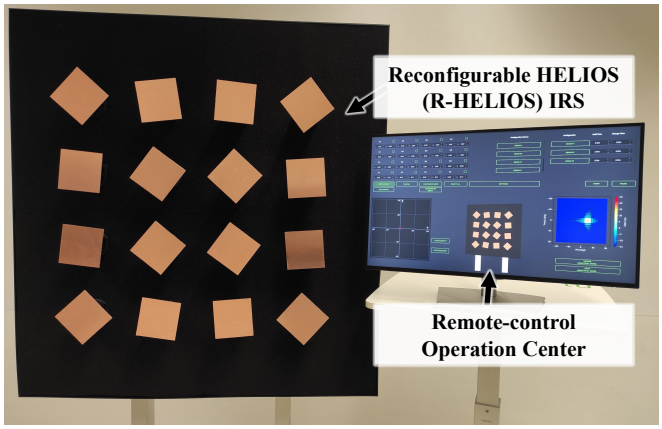

FIGURE 4. **Developed research platform. *(left)* Depicted mmWave IRS extends prior static HELIOS concept by mechatronical reconfiguration capability [39]. *(right)* Complementary remote control operation center integrating 6G network side functions during measurement campaigns.**

R-HELIOS implementation is to leverage servomotors upon which reflecting surfaces are mounted to realize the dynamic beamsteering capability [160]. We build up a 16-element IRS with a 4×4 module arrangement, each with a $10\,\mathrm{cm} \times 10\,\mathrm{cm}$ footprint. The overall design concept is illustrated in Fig. 2 along with the control circuitry.

Module Assembly: The mechanical reconfiguration of the reflecting surface is attained using pan and tilt motors [161] to attain the desired horizontal and vertical tilt angles α and β. The servomotors are stacked and complemented by a custom 3D-printed stabilizing holder system structure, as shown in Fig. 3a. The module attains the full beamsteering capability, i.e., $\alpha, \beta \in [-90°, 90°]$. Therefore, azimuth- and elevation-plane reflection angle changes of 2α and 2β, reaching up to 180°, can be realized according to the natural law of reflection for the tilted reflecting surface [54]

$$\phi_{out} = -\phi_{in} + 2\alpha \text{ and } \theta_{out} = -\theta_{in} + 2\beta. \tag{2}$$

On top of the C-bracket of the upper servomotor, we attach the reflecting surface. A single layer of adhesive copper tape [162], typically used for EM interference suppression, is applied to the additively manufactured body. One complete module is presented in Fig. 3b, showing two different reflection alignments. The switching between configurations is quick with an angular velocity of 0.375 °/ms [161]. The modules are mounted with a center-to-center inter-module spacing of approximately 19 cm which allows for collision-free operation of the modules regardless of the orientation of the neighboring modules. We discuss deployment-specific optimization aspects for this in Sec. III-B. Moreover, we add EM absorbers [163] behind the reflecting surfaces to mitigate undesired reflections from the R-HELIOS IRS system.

Module Control: We employ an SBC [164] to control the 32 servomotors. Additionally, two 16-channel pulse-width modulation (PWM) controllers [165] are employed as de-multiplexers to overcome the limited number of input/output-pins of the SBC. Based on digital inputs from the SBC,

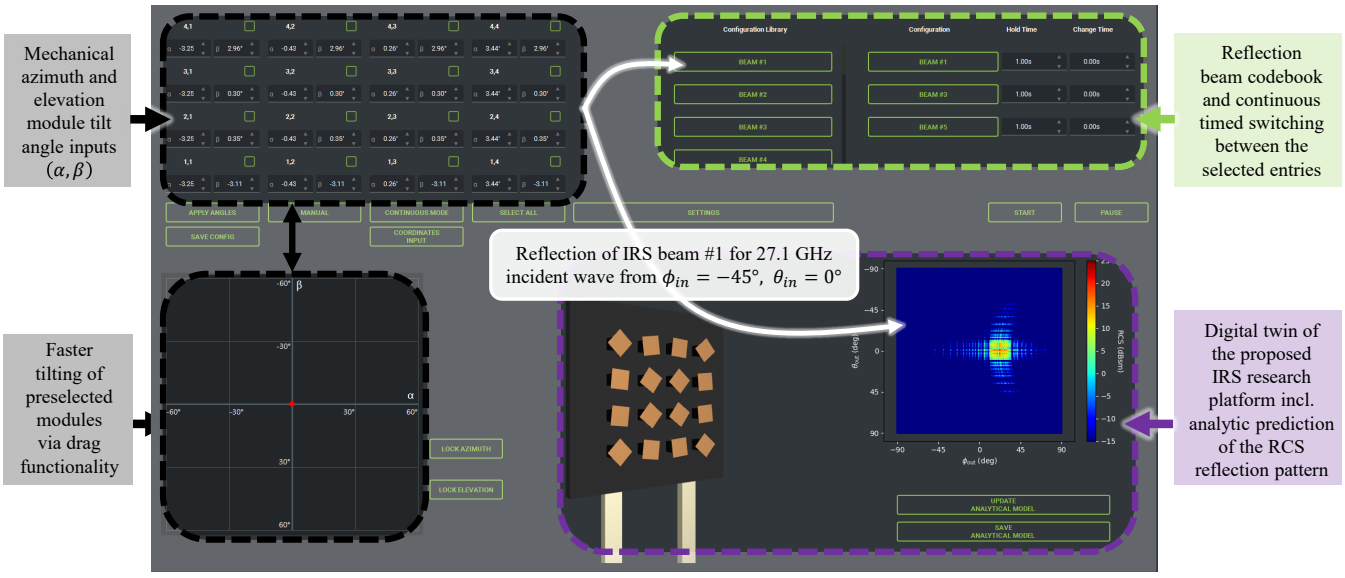

FIGURE 5. **IRS real-time control and orchestration functions accompanied by a digital system twin. *(left)* Reflection beam codebook entry generation by tuning of azimuth and elevation tilt angles of the 16 modules. *(top right corner)* Reflection beambook and continuous timed switching between selected entries. *(bottom right corner)* Visualization of the current R-HELIOS state accompanied by the predicted far field reflection pattern [54].**

each of the two controllers generates 16 analog 12-bit PWM signals to set the angle of the connected 16 servomotors, i.e., 8 modules, in dependency of the PWM duty cycle. Two input/output-pins of the SBC are used by the inter-integrated circuit (I^2C)-bus for the communication with the PWM controllers. For these reasons, a printed circuit board (PCB) was designed to provide the required electrical connections as well as the mechanical attachment of the hardware components. The basic concept of the PCB can be seen on the left side of Fig. 2, which moreover sketches the serial data (SDA) and serial clock (SCL) lanes of the I^2C-bus. With the above described control circuitry, we can simultaneously steer all 16 modules. The mechanic tilt actuation tuples (α_k, β_k) with $k = 1, \ldots, 16$ can be remotely supplied to the SBC.

IRS Remote Control and Reflection Orchestration Function

The reconfigurable IRS, specifically the SBC component, is connected to our operation control center via a wireless control link in the sub-6 GHz spectrum. Both components are shown together in Fig. 4 for a broadened reflection with 10° beamwidth [54]. The main functionality of the control center described in this section are reconfigurations of the overall reflection characteristics of R-HELIOS over time. For this reason, it provides functionality to add new beam codebook entries by optimizing the tilt parameters of all modules, see left side of Fig. 5. The angles can either be set numerically for each module (top left corner) or by using a click-and-drag field (bottom left corner). Another method employed in this work is the generation of beam configurations based on scenario details (cf. *settings* button), such as distances $d_{\text{BS,IRS}}$ and $d_{\text{IRS,UE}}$ to the communication nodes as well as azimuth and elevation angles of incidence and departure, respectively. All saved beam configurations of the beambook can be integrated into the continuous beamsweeping process with predefined timings, cf. top right corner of Fig. 5. We employ this function for the exhaustive IRS beam searches in Sec. IV-B and for beam tracking in Sec. IV-C. These above-described functions of the control center are assisted by a digital twin, shown in the bottom right corner of the figure, depicting the current geometric state of the IRS along with the reflection behavior in the form of an angular RCS heatmap leveraging the analytical model from [54]. The implementation of the control function for our experimentation is mainly based on the Python `Qt` and `Qt3D` packages [166].

We provide both in-depth IRS assembly instructions and the module control code in [32] to facilitate the recreation of the mechatronically reconfigurable IRS research platform and performance studies similar to our trials in Sec. IV.

B. Laboratory Validation and Future Potentials

Calibration: Initial measurements with a digital angle gauge [167] showed that reflecting surface misalignments of up to 15.7° can occur in certain directions. Therefore, the R-HELIOS was calibrated following the concept shown in Fig. 6a. Each servomotor was measured for the tilt angles of −90°, 0°, and 90°. At these angles, direct calibration is applied reducing misalignments to less than 0.5°. This method, however, could not be applied for any other arbitrary angle $\Psi \in [-90°, 90°]$ due to infeasible overhead. The intermediate angular range is therefore calibrated by using the previously attained calibration values, referred to as value A at angle 0° and B from ±90°, with the sign depending on the sign of the desired steering angle Ψ. The calibration formula in Eq. (3) calculates the calibration value $C(\Psi)$ with a weighting factor depending on angular separation to the

previously calibrated steering angles.

$$C(\Psi) = A \cdot \cos^2(\Psi) + B \cdot \sin^2(\Psi) \tag{3}$$

Against this background, systematic measurements of various tilt angles Ψ of all 32 calibrated servomotors yield a peak absolute deviation of $\Delta\Psi_{max} = 1.27°$. However, the mean error of more than 480 measurements with the digital angle gauge [167] for uniformely distributed tilt angles is $\Delta\Psi_{\mu} = 0.03°$ with a standard deviation of $\Delta\Psi_{\sigma} = 0.47°$. The empirical distribution is depicted on the left side of Fig. 6b.

Misalignment Loss: We determine the power loss based on the previously established empirical distribution of the module surface misalignments. For this step, we consider the RCS reflection pattern $\sigma(\phi_{out}, \theta_{out})$ of a single module at 28 GHz as predicted by EM simulations with `Ansys HFSS` [168] as shown in Fig. 6b. The peak reflection angle is at the azimuth angle $\phi_{out} = -\phi_{in} + 2(\alpha + \Delta\Psi_{az.})$ and elevation angle $\theta_{out} = -\theta_{in} + 2(\alpha + \Delta\Psi_{el.})$ [39, 54]. For brevity, we consider a deployment scenario with a boresight angle of incidence $(\phi_{in} = \theta_{in} = 0°)$ and the R-HELIOS state with no mechanic tilt $(\alpha = \beta = 0°)$. In this case, the peak reflection angle is only dependent on the misalignment of the horizontal and vertical tilt angles: $\phi_{out} = 2\Delta\Psi_{az.}, \theta_{out} = 2\Delta\Psi_{el.}$. In the worst case, it holds $\Delta\Psi_{az.} = \Delta\Psi_{el.} = \Delta\Psi_{max}$ for which we observe a maximum loss of 5.2 dB. However, considering the measured empirical distribution for $\Delta\Psi_{az.}$ and $\Delta\Psi_{el.}$, the mean power loss by module misalignment is 0.7 dB which is small compared to the peak RCS, see on the right side of Fig. 6c. Moreover, there is less than 1 dB power loss in about 74.3 % of IRS module alignments making R-HELIOS efficient when compared to implementation losses of 3.1 dB to 5.8 dB reported for the IRSs in [25, 83, 146].

Assessment of Reflection Metrics: We further employ the RCS solver of the simulation software [168] to assess the far-field reflection for a beamformed reflection configuration at 27.1 GHz like in Sec. IV. Considering the previously described module parameters, a peak RCS value σ_{max} of 34.2 dBsm is expected at normal incidence and may thus be used to estimate the received power of the hereby provided reflection path according to Eq. (1). In practice, however, the reflection gain is monotonically decreasing with the absolute value of the required angles of incidence and departure. Additionally, we note that the geometry of R-HELIOS may also induce self-shadowing effects at large tilt angles, thereby reducing the RCS further [54].

Moreover, considering the vertical and horizontal edge-to-edge inter-module spacings of 8.76 cm and 9.1 cm, the following half-power beamwidths are extracted from the attained reflection pattern: 0.73° vertically, 0.76° horizontally. The 10 dB-beamwidth is 3.2°. We note that there are some grating lobes in the reflection pattern owing to the unavoidable inter-module spacings, however, the dominant fraction of the total reflection power is contained in an about $7.1° \times 7.2°$-sized angular area centered around the main lobe.

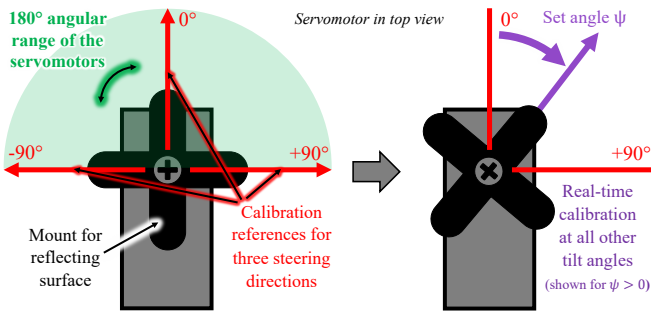

(a) Live calibration for arbitrary steering angles Ψ leverages calibration values of the center and boundary angles of the 180° range.

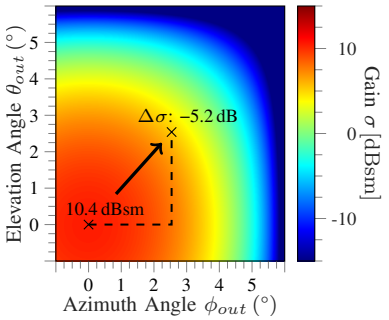

(b) Simulative study of the power loss incurred with worst-case misalignments.

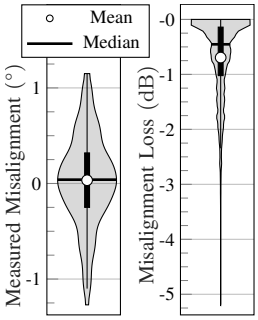

(c) Power loss for the misalignment distribution.

FIGURE 6. Calibration of mechanical module tilting for low power losses.

In terms of supported bandwidth of the IRS system, we refer the reader to our prior work [140] which found that the static flavor of R-HELIOS exhibits a bandwidth beyond 10 GHz in the mmWave spectrum. In particular, the 800 MHz wide spectrum (26.7 GHz to 27.5 GHz) of the 5G FR2 band n257, which is used by our mmWave communication system in Sec. IV, is fully included.

R-HELIOS Power Consumption: A power measurement device [169] is used to assess the power demand of the developed IRS, as shown in Fig. 7. In a static configuration state, the 5 V-driven IRS platform draws a current of 265 mA, resulting in about 1.3 W power consumption for the control circuitry (mainly the SBC). When switching between IRS configurations, the power consumption is highly dynamic with strong dependence on how many modules are actuated. For example, measured peak values for switching one to three modules are 2.5 W, 3.7 W, and 5.2 W, respectively. We observe a peak power consumption of 31.1 W when simultaneously switching all 16 modules, requiring activity by all 32 servomotors, two PWM controllers, and the SBC. We note that the 31.1 W peak power consumption could be decreased to 2.5 W by switching the IRS modules sequentially instead of simultaneously. Overall, we note that the baseline power consumption is still similar to that of mmWave modems in the connected state without payload traffic (ca. 1.5 W to 2.3 W) [170, 171], but much smaller than the consumption of full-blown BSs.

Compared to the mmWave RISs in Tab. 1, our IRS is more efficient than [44, 149, 153, 172] with peak power

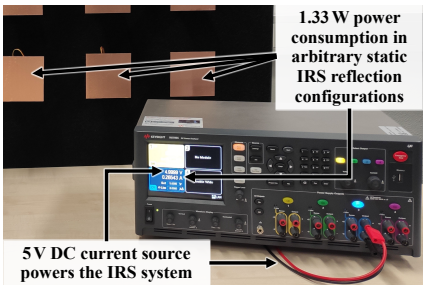

FIGURE 7. **Laboratory setup for IRS power consumption measurements during a static reflection state, shown in photo, and beam switching.**

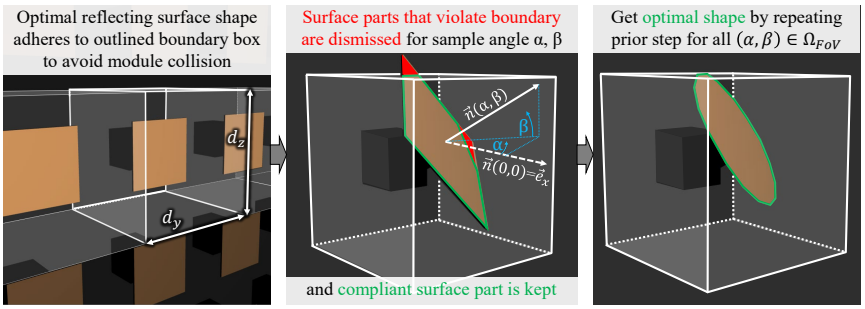

FIGURE 8. **Module shape customization according to the available unit cell space and specified mechanical tilt angle range.**

consumption levels between 35 W to 234 W. This is despite smaller effective reflecting surface areas, except for [153]. Minimum and typical power consumption values in [44, 138, 144] are similar to the ones of our research platform. More efficient mmWave IRSs have been reported, however, some with a less efficient power consumption per reflecting area [69, 71, 90]. Against this background, IRSs [24, 64, 70, 134, 173] could be more beneficial in highly-dynamic multi-user scenarios requiring regular IRS reconfiguration activities, whereas R-HELIOS is more suitable for occasional beam switching and tracking events. Considering the above performance values and that it is typically not reported (cf. Tab. 1), we attest positive power consumption characteristics compared to most mmWave IRSs.

Toward Custom Module Shapes and Spacings: This work leverages planar rectangular $10\,\mathrm{cm} \times 10\,\mathrm{cm}$ modules for compatibility with the reflection model in the remote control center, whereas, for example, curved rectangular reflecting surfaces have already been successfully tested in [140]. Our module arrangement leverages empty spaces between the modules such that neighboring modules cannot collide if steered toward one another. This paragraph gives insights into potential improvements in these aspects. In essence, collisions can be avoided if the angular module tilt space is constrained. This may be a natural limitation that can be derived from the IRS deployment scenario, for example, a small range of vertical and horizontal tilt angles may be sufficient to dynamically illuminate an urban street canyon. Incorporating such field of view (FoV) restrictions in the proposed IRS would allow for reduced inter-module spacing. Alternatively, the module surface area can be shaped according to the desired module spacings $d_y \geq a$ (width), $d_z \geq b$ (height) and angular FoV $\Omega_{\mathrm{FoV}} \subseteq [-90°, 90°]^2$ requirements as shown by Fig. 8. Given the highlighted module-specific bounded space on the left subfigure, the surface of the module shall be tailored. For this reason, all steering angles $(\alpha, \beta) \in \Omega_{\mathrm{FoV}}$ are probed as shown in the middle of Fig. 8. Therein, it is sketched that surface parts that exceed the predefined boundary (see red highlighted surface parts) need to be removed whereas the conformal surface region (see green polygon) is kept. By repeating this process for all steering tuples, the optimal surface is identified. As shown on the right side of the figure, a circular shape emerges (instead of an rectangular shape) if the FoV is not constrained. In that case, the reflecting surface area would be about 78 % larger so that the peak RCS for each module increases by 217 % (i.e., +5.0 dB), cf. Sec. II-A. An irregular shape arises for the service area in Sec. IV-C with 5.8 dB gain compensating the remaining worst-case misalignment losses. However, this measure is not leveraged at this point due to unpredictable interactions between the modules' reflection sidelobes.

IV. FIELD TRIALS OF MECHANICAL IRS-ASSISTED BLOS MMWAVE COMMUNICATIONS TOWARD 6G

This section transfers the developed R-HELIOS IRS into a real mmWave deployment to improve connectivity in NLOS areas. Sec. IV-A presents the measurement setup and methodology for our study. Thereafter, Secs. IV-B and IV-C study selected aspects of IRS-aided wireless communications (cf. Sec. II-A) in indoor and indoor-to-outdoor scenarios.

A. Measurement Methodology

We introduce the methodology for our measurement campaigns in two steps. First, the mmWave communication equipment is introduced along with overall deployment scenario details. This is followed by details on the physical channel to application layer parameter acquisition.

mmWave Communication System and Environment: Tab. 2 summarizes the key configurations of the deployed 5G non-standalone (NSA) mobile radio network operated in E-UTRAN / NR dual connectivity (EN-DC) mode. The mmWave cell operates with the center frequency of 27.1 GHz using 800 MHz of bandwidth. The antenna array of the mmWave cell is attached to a pole at the edge of the hall with a center height of 3.1 m. We have set the transmit power such that an equivalent isotropic radiated power (EIRP) of 25 mW is not exceeded. Moreover, the network is configured to enforce payload data transmission in FR2. In our trials, we employ three off-the-shelf UEs with cross-polarized 8×8 antenna arrays that are typically placed in NLOS modality.

The private network is deployed in an indoor factory (InF)-like hall in the vicinity of the TU Dortmund University campus. Industry-typical objects such as safety cages lead to strong EM shielding. In the scope of the indoor study

in Sec. IV-B, we place two UEs therein whereas the third UE in LOS. The trial environment is moreover extended in Sec. IV-C by placing the mobile UE outside the hall with the antenna array center at a height of 1.3 m. There, the LOS modality is prohibited by the concrete building walls plus storage shelf system-like metallic obstructions before the windows on the inside, however, an artificial propagation path shall be introduced through a factory-scale hall gate. Figs. 10 and 15 show the two considered deployment scenarios with in-depth details being supplied in the respective field trials, Secs. IV-B and IV-C.

Acquisition of Performance Metrics: We employ the so-called spatially distributed traffic and interference generation (STING) concept [174] which was proposed for technology-independent wireless network stress testing under real world conditions via distributed devices. In its current form, UE and BS side parameters are provided with 1 s time resolution in the network companion [13]. In this work, we focus on the synchronization signal reference signal received power (SS-RSRP), rank indicator (RI), synchronization signal block (SSB) beam index, and user datagram protocol (UDP) throughput parameters which are acquired for UL and DL transmissions, respectively. The mean values in Secs. IV-B and IV-C are extracted from 60 s measurement data from which the first and last 15 s are discarded.

TABLE 2. Overview of IRS-assisted 5G NSA / EN-DC network [77].

	Parameter	Description/Value
Cell Configurations	**FR1 / LTE Anchor Cell**	
	Radio Unit	Ericsson Radio 2203
	Frequency Band	LTE band 7 (FDD)
	Center Frequency	2.65 and 2.53 GHz (DL/UL)
	Bandwidth	20 MHz (10 MHz/10 MHz)
	Transmit Power	100 mW (EIRP)
	FR2 / NR mmWave Cell	
	Radio Unit	Ericsson AIR 1281
	Frequency Band	NR n257 (TDD)
	Frequency Range	26.7 to 27.5 GHz
	TDD Pattern	DDSU, 11:3:0
	Bandwidth	800 MHz using 8× 100 MHz and 120 kHz Subcarrier Spacing (SCS)
	Transmit Power	25 mW (EIRP)
	Mounting height	3.1 m at center of antenna
User Equipments	# Devices	Up to three UEs, typically in NLOS
	Device Model	Quectel 5GDM01EK with Quectel RG530F-EU
	Modem	Qualcomm SDX65
	mmWave Antenna	Qualcomm RA530T with 4× QTM547 (8×8, cross-polarized)
	LTE Category	Cat 20 / Cat 18 (DL/UL)
	5G NR Compliance	Release 16 NSA/SA
	Power Class	Class 3 (23 dBm)
	MIMO Capabilities	FR1: DL 4×4, UL 2×2 FR2: DL 2×2, UL 2×2
Intelligent Reflecting Surface	Architecture	Mechanically reconfigurable HELIOS using 3D-printed modules with conductive coating
	Design Layout	4×4 modules, $40\,\mathrm{cm} \times 40\,\mathrm{cm}$ effective area
	Performance Metrics	34.2 dBsm peak radar cross section (sim.) 3.2° 10 dB-beamwidth (sim.) Static beam power consumption: 1.3 W (meas.) Peak power during switching: 31.1 W (meas.)
	Mounting height	1.825 m at center of IRS
	3D Distance to FR2 cell	11.4 m (Sec. IV-B), 23.4 m (Sec. IV-C)
	3D Distance to UEs	3.2–4.3 m (Sec. IV-B), 4.8–12.3 m (Sec. IV-C)

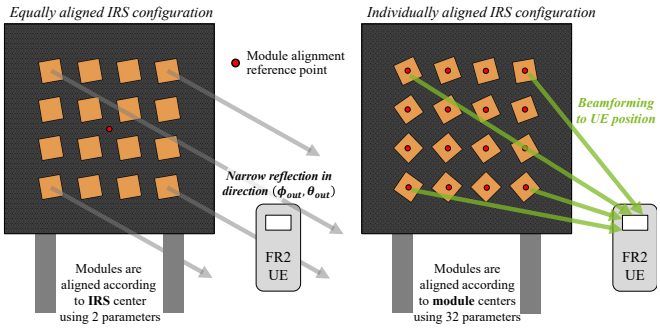

FIGURE 9. Considered reflection beam configuration: *(left)* All modules have same surface 3D tilt vs. *(right)* individual module alignments.

We note that the maximum throughput is upper-bounded to 2 Gbit/s as in [77] to prevent fluctuations in the measurement data. In regards of the UL throughput performance we note that a time division duplex (TDD) pattern is employed which favors DL-heavy applications. Moreover, the UEs only support 400 MHz transmission bandwidth which further constrain the UL throughput to a maximum value of about 650 Mbit/s. The value range of RI is $[1, 2]$ as there is support for two MIMO layers. The minimum supported SS-RSRP is between −110 dBm to −105 dBm leading to an abysmal data rate and high chance for mmWave link failure. Peak data rates are attainable for signals exceeding about −90 dBm received power depending on the leveraged number of spatial streams.

Measurements are performed *with* and *without* the proposed IRS from Sec. III. The entire reflecting area of R-HELIOS is always in LOS of the mmWave cell and the UEs. Moreover, in some measurements the IRS reflection beam is deliberately *misaligned* (typically all 16 modules) to assess the impact of transferring the IRS platform into the radio environment. During the measurements, we use two different types of beams to realize a smart mmWave environment, as shown in Fig. 9. The first beam type, to which we refer as *equally aligned*, leverages the same mechanical tilt defined by (α, β) for all modules, cf. left side of figure. On the one hand, the tilt angles are geometrically obtained using the center of the IRS as the alignment center. On the other hand, we also consider an exhaustive beam search to identify suitable tilts. For the second beam type, *individually aligned*, the individual mounting positions of each module are considered. This results in individual module tilt angles $(\alpha_k, \beta_k), k = 1, \ldots, 16$, see right side of figure. Our expectation is that this results in a better performance at cost of a more complex training procedure in practice.

It can be calculated that the far-field distance of our large-scale IRS begins at 28.9 m. Therefore, our measurements take place in the near field. The consequences for the

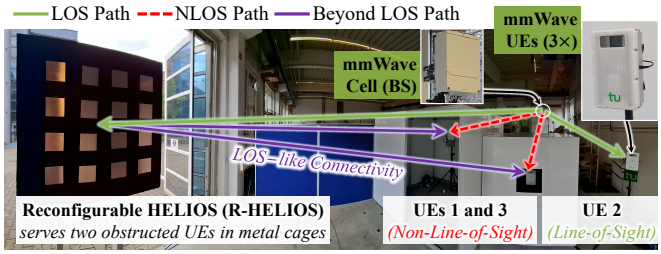

(a) InF-motivated IRS use case with UEs in EM-shielding safety cages.

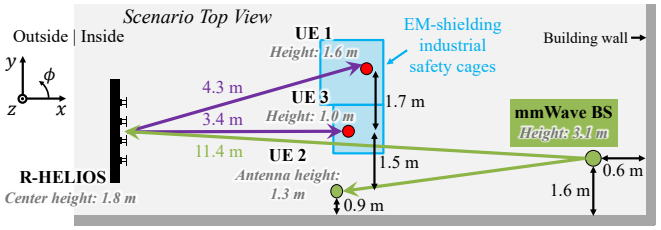

(b) Top view sketch of indoor measurement scenario.

FIGURE 10. Indoor evaluation scenario: mmWave deployment uses IRS for multi-user BLOS communications and IRS beam training testing.

reflection characteristics are a broader and weaker reflection for the *equally aligned* beams, cf. [175]. Owing to the UE position-centric alignment of the modules in *individually aligned* beam configurations, a parabolic reflector is imitated with the UE being at the focal point. Therefore, these beams realize near-field beamfocusing providing larger gains.

B. Indoor Measurements

Scope and Setup

Fig. 10 provides a photo of the indoor-oriented deployment scenario in *(a)* and numeric details with the site plan in *(b)*. In this scenario, three static UEs are deployed. UE 2 is in LOS of the mmWave cell with a 3D distance of 8.7 m. This communication link will serve as the reference to compare the links of the other two UEs with: UE 1 is placed in an industrial shielding cage, specifically a regular cuboid with 2.0 m side lengths, which significantly weakens the LOS propagation path, cf. [77]. However, the metal cage has an entrance of $2.0\,\mathrm{m} \times 1.0\,\mathrm{m}$ through which an IRS could provide an artifical propagation path. Similarly, UE 3 is also placed in an industrial shielding cage with a size of $1.4\,\mathrm{m} \times 1.4\,\mathrm{m}$ and height of 1.6 m. The opening of this cage is significant smaller with a 30 cm by 30 cm window, cf. [13], requiring a well-aligned IRS reflection.

The R-HELIOS IRS is placed in a 3D distance of 11.4 m to the mmWave cell with a center height of 1.8 m. The azimuth and elevation angles of the incident wave from the mmWave cell at the center of the IRS are $\phi_{in} = 3.37°$ and $\theta_{in} = 6.30°$. Different vertical tilts are required for the three UEs which have been intentionally positioned at different heights: UE 1 at 1.6 m, UE 2 at 1.3 m, and UE 3 at 1.0 m. Because they are placed at different x-y-positions, the horizontal tilts are also unique. The 3D distance from the IRS center to UE 1 is 4.3 m and 3.4 m for UE 3.

Against this background, the goal of this setup is to study physical channel to system level parameters on single- to multi-user connectivity with and without IRS providing one or multiple reflection beams. Moreover, insights on IRS beam training toward future autonomous reflection configuration for distributed UEs are attained.

Results and Discussion of Indoor Measurements

User Connectivity without IRS: The baseline connectivity is established at first. We note that the IRS system is not even physically in the scenario for this. Moreover, only one user is active at a time. In this situation, the LOS UE 2 achieves the full UDP throughput in the DL with 1.97 Gbit/s and 0.66 Gbit/s in the UL. An SS-RSRP of −74 dBm is obtained in both link directions together with a RI of 2.00, underlining the availability of multiple strong and stable propagation paths. The LOS performance of UE 2 is considered with dashed purple lines in Fig. 11.

Moreover, Fig. 11 presents the NLOS UL/DL performance of UE 1 in *(a)* and UE 3 in *(b)*. Without IRS, UE 1 achieves a DL throughput of 0.41 Gbit/s (−79.2 % vs. UE 2) and 0.31 Gbit/s in the UL (−53.0 %), based on −100 dBm SS-RSRP. Compared to UE 1, UE 3 experiences a better NLOS throughput of 0.84 Gbit/s in the DL and 0.57 Gbit/s in the UL despite the smaller opening in the shielding cage. This is because there is an additional propagation path from a distant wall behind the later IRS position. This is confirmed by the RI: for UE 3 it is on average 1.70, whereas only 1.05 for UE 1. Overall, we attest a drastically reduced performance of the NLOS UEs $\{1, 3\}$ in comparison to LOS UE 2.

Improving Connectivity with R-HELIOS IRS: To achieve improvements in the connectivity performance, the IRS is brought into the scenario, however, at first with a misaligned reflection beam toward the ceiling ($\beta = 45°$ uptilt, $\alpha = 0°$), as shown in Fig. 12a. Studying the respective impact on the single-user connectivity levels of the NLOS UEs in Fig. 11, mean throughputs and SS-RSRP increase slightly, e.g., there is 1 dB more received power as we have essentially introduced a scattering object in the radio environment. However, the poor connectivity level remains.

In a next step, we assess the performance gain by using an equally aligned beam configuration (cf. left side of Fig. 9) toward UE 1. Fig. 11a shows the significant positive impact on the communication link in the form of an increased DL throughput of 1.75 Gbit/s (+1.22 Gbit/s) and realization of the peak UL throughput of 0.66 Gbit/s (+0.37 Gbit/s). The reason for this is that the created propagation path increases the SS-RSRP by 16 dB while also realizing a stable RI of 2.0. We observe a similar behavior for UE 3, cf. Fig. 11b. The DL throughput increases by 0.98 Gbit/s to 1.86 Gbit/s and the UL throughput is also maximized. Hence, both UEs now have nearly LOS-like connectivity in terms of application throughput. However, the SS-RSRP of UE 3 only increased by 6 dB. One potential reason for this is the small opening of the metal cage in combination with a simple IRS

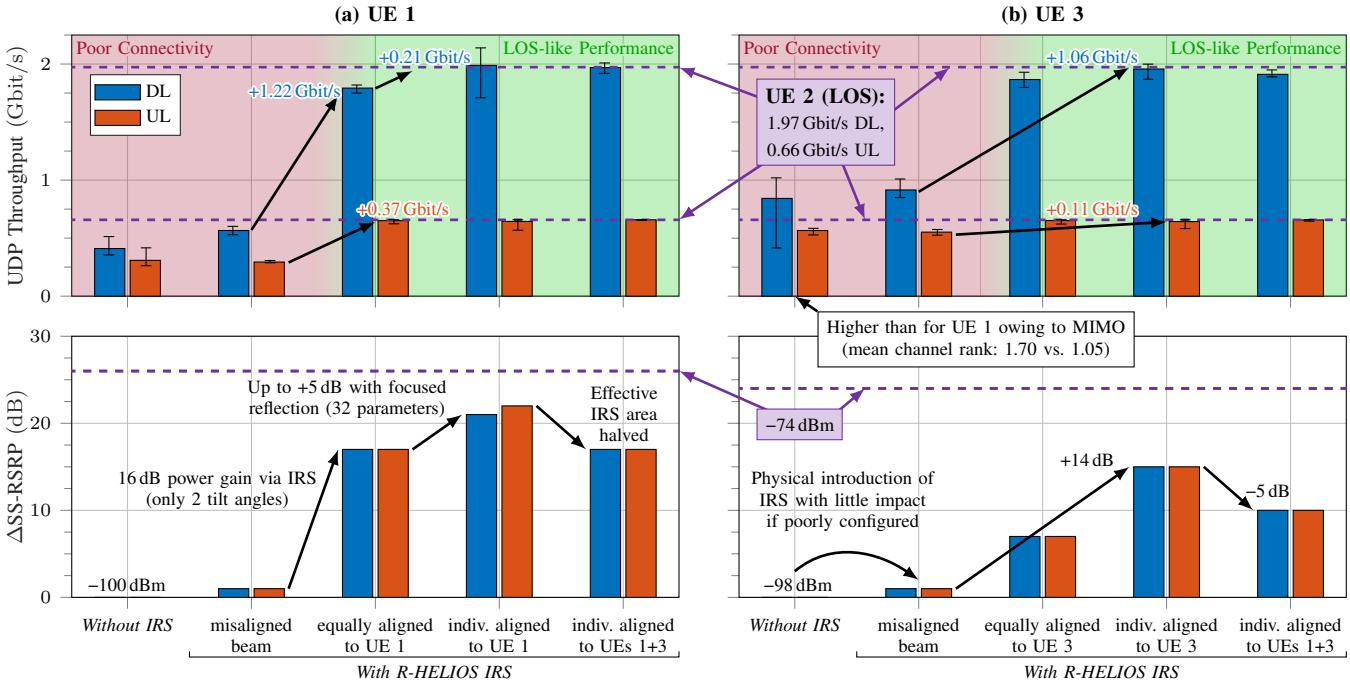

FIGURE 11. **Impact of R-HELIOS IRS on single-user UL/DL throughputs and SS-RSRP for *(left)* UE 1 and *(right)* UE 3. No other UE is connected during the respective measurements. Reference performance of LOS-situated UE 2 depicted in purple.**

configuration which, owing to the UE being in the near-field of the IRS, directs a comparatively broad reflected EM wave into the desired direction rather than under far-field conditions.

Therefore, we now switch to reflection beams wherein each IRS module is individually aligned to focus the reflected EM waves at the intended UE position (cf. right side of Fig. 9). The resulting IRS configurations are shown in Figs. 12b and 12c. Back in Fig. 11 we study the impact of this measure: both UEs now also attain the peak DL throughput at about 2 Gbit/s, just like the other UE placed in LOS modality. This is founded on further SS-RSRP increases: by 5 dB for UE 1 and 8 dB for UE 3. Referring back to the previous paragraph, this confirms that the individually aligned beams are clearly better suited to serve the UEs.

We briefly compare the previous measurement results to selected related works. Similar to the measurement campaign in an indoor train station hall with a public mmWave network in [44], we can confirm that switching between reflection configurations with different beamwidths indeed has an impact of at least 5 dB on the end-to-end communication link. Moreover, we also corroborate the observed peak gains of 22 dB using a focused reflection beam configuration. Our results furthermore showcase that throughput gains are not upper-bounded to 55 %, cf. [44], but may be as high as 271.7 %. Considering absolute values, we also cross-validated mmWave IRSs-enabled throughput gains of several hundred Mbit/s as in [55].

IRS Size Sensitivity Analysis: As noted in Sec. II-A, the received power of a BLOS propagation path depends on the effective IRS surface area squared when neglecting other communication system effects, such as modulation and coding scheme (MCS) adaptation and transmit power control. In the scope of network planning before IRS deployment, it is an important aspect to determine how large the IRS ought to be. Even when a sufficiently large IRS has already been rolled out, partial use of the unit cells is of high interest, either to serve multiple users simultaneously or to reduce IRS power consumption if the BLOS link with the entire IRS exceeds quality of service (QoS) requirements. For these reasons, we study the impact on UE 3 connectivity when misaligning modules one after another until the misaligned R-HELIOS configuration is attained, cf. Fig. 12a. The results are presented in Tab. 3 as performance delta against the full-blown BLOS connectivity level, cf. Fig. 12c:

We find that the throughput remains constant as long as at least 6 modules, i.e., a reflecting surface area of 600 cm^2, is employed. Considering that the RCS of flat conductive surfaces is proportional to the squared reflecting surface area [54], one would expect an SS-RSRP degradation of up to about 8.5 dB. Additional trials with a different module misalignment order have yielded the same result. We have also observed similar behavior for UE 1. Hence, other system characteristics, such as BS-side transmit power control, could be a reason for the observed behavior.

Continuing with the step-wise misalignment process of the R-HELIOSs modules, an impact on the connectivity of UE 3 is observed: With 5 remaining modules the SS-RSRP deteriorates by 4 dB. Misalignment of more modules reduces the SS-RSRP further, however, in that case also with impact

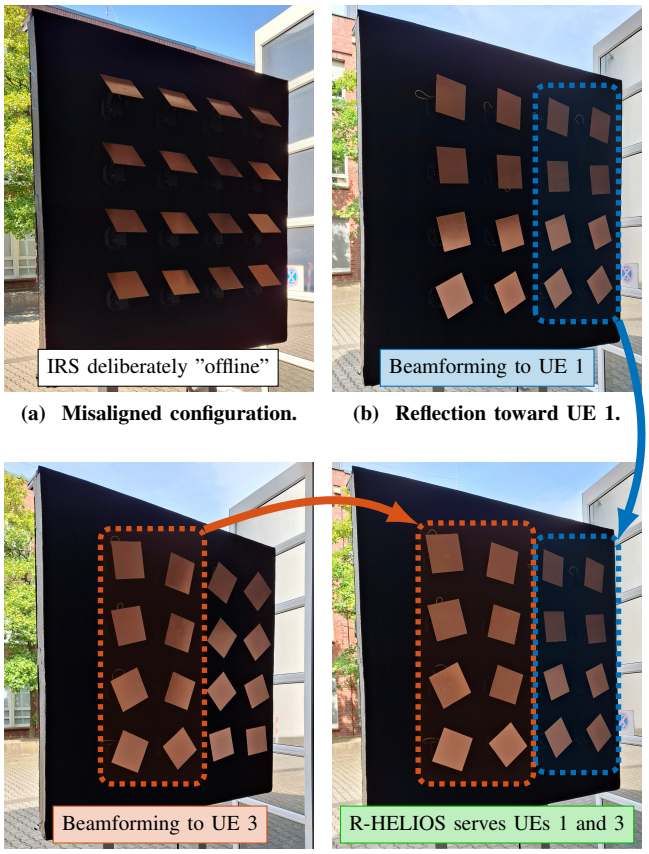

(a) Misaligned configuration. (b) Reflection toward UE 1. (c) Reflection toward UE 3. (d) Multi-armed beam.

FIGURE 12. IRS configurations during measurements of Figs. 11 and 13. In *(b)–(d)* all of the modules are individually tilted toward the NLOS UEs.

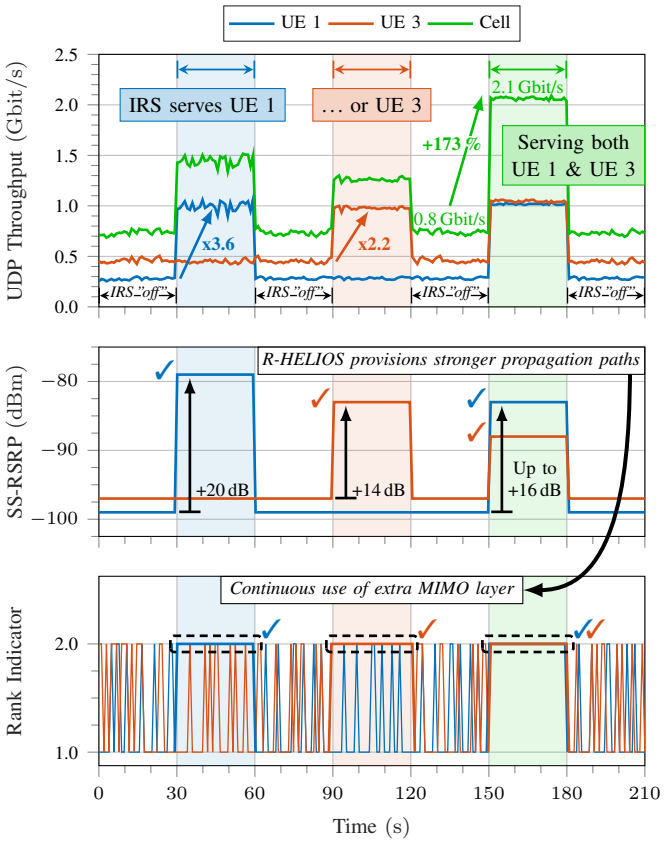

FIGURE 13. Impact of R-HELIOS IRS on simultaneous DL transmission of NLOS-situated UEs $\{1, 3\}$. Under a fair physical resource sharing regime, user- and cell-level performance can be maximized when serving the NLOS UEs with a custom-tailored multi-armed reflection.

on the DL data rate. We conclude that with some minor impact on the link quality, the proposed IRS could be large enough to support up to four UEs by assigning four of 16 modules, respectively.

Multi-user Connectivity: Considering the insights from the previous paragraph we now split the reflecting surface into two sub-arrays with 8 modules, respectively. One sub-array serves UE 1 and the other UE 3, see Fig. 12. For this configuration, we again first study the performance that only one UE is active at a time, see Fig. 11. We observe a loss in SS-RSRP of 4 dB to 5 dB. The UL throughput nonetheless remains unaffected. The peak loss in DL direction is 45 Mbit/s and thus negligible when exchanging payloads with about 2 Gbit/s.

In the following paragraph, we now study the performance for the different individual beam alignments depicted in Fig. 9 when both NLOS-situated UEs are actively receiving DL payload data. The R-HELIOS is set to switch between the beambook entries every 30 s with the measured link metrics of the 3.5 min measurements depicted in Fig. 13. In the intentionally misaligned IRS configuration both devices attain a joint throughput of about 0.75 Gbit/s constituting the mean of the respective single-user measurements. This is in line with our previous work [77] wherein we observed a fair physical resource scheduling between multiple UEs in LOS. Moreover, in regards of the RI metric, we observe that it oscillates between 1 and 2, indicating that there is no sufficient second propagation path to leverage a second MIMO layer. When now configuring the IRS to serve only UE 1, the data rate of UE 3 remains unaffected, whereas UE 1 approximately doubles its throughput to 1 Gbit/s. Also, we observe that the RI is now stable at value 2 which underlines that the second MIMO layer is now continuously in use, however, only for the IRS-assisted UE. Similar behavior is observed when serving UE 3 exclusively with the IRS. The performance for the multi-armed reflection beam case is most interesting with both UEs attaining a DL throughput of more than 1 Gbit/s, respectively. Similar to [77], the cell throughput now exceeds 2 Gbit/s. Overall, the mean cell

TABLE 3. Sensitivity analysis to leveraged number of reflecting modules. Connectivity level of UE 3 is maximized with less than 50 % of available reflecting surface.

Number of Aligned R-HELIOS Modules	16–6 (BLOS)	5	4–3	2–1	0 (NLOS)
ΔThroughput (Gbit/s)	0	-0.03	-0.13	-0.45	-1.07
ΔSS-RSRP (dB)	0	-4.0	-8.0	-8.0	-14.0

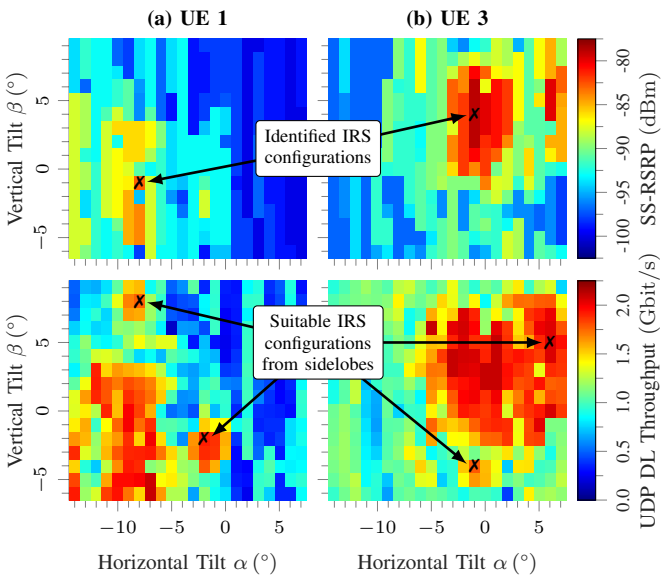

FIGURE 14. Exhaustive search performs systematic beam sweeping leveraging respective tilts (α, β) of the reflector modules. IRS configurations that optimizes the BLOS link, either in terms of UDP DL throughput or SS-RSRP, can be successfully identified.

throughput over this 30 s period is increased by about 173 % (+1.25 Gbit/s) against the performance without any IRS assistance. This outlines that the mmWave IRS is therefore not only a measure to improve connectivity of individual users but that the network operator also benefits from the deployment because the overall network efficiency is increased.

IRS Beam Training: Thus far, suitable IRS states were geometrically derived which is typically not feasible in mobile radio networks. mmWave and IRS-assisted networks leverage beam management to align antenna and reflector beams. In this work, the BS and UE beam management is a blackbox which quickly adapts to the current state of the radio environment based on regular control signaling, as observed by the rapid and seamless connectivity changes in Fig. 13 depending on the current IRS state. Against this background, we investigate beam training to align the ideal IRS configuration, however, we employ the subpar equally aligned type (instead of individually aligned reflection beams, cf. Fig. 9) because this reduces the number of parameters that have to be identified down to just two. Future work may consider a subsequent beam refinement stage to identify a suitable reflection beam using 32 parameters for additional gain.

We conduct a slow exhaustive beam search by sweeping (α, β) through the angular space $[-14°, 7°] \times [-6°, 9°]$ with an angular resolution of 1°. Each direction is observed for 6 s for which mean SS-RSRP and DL throughput values are determined. In total, 352 directional link states are measured for both NLOS UEs as depicted in Fig. 14. We first study the beam search for UE 1 in *(a)* with the SS-RSRP displayed at the top and the application data rate at the bottom. For the latter, it can be clearly observed that one configuration, i.e., $(\alpha, \beta) = (-8°, -1°)$, outperforms all others by at least 2 dB. In practice, however, several configurations attain the same data rate below 2 Gbit/s, for example, using reflection sidelobe from the beams aligned in the regions around $(-2°, -2°)$ and $(-8°, 8°)$. Similar behavior is observed for UE 3 in Fig. 14b but with a larger feasible angular region attaining high performance deltas compared to misaligned IRS states. Overall, with peak SS-RSRP gains of 17 dB and 19 dB, respectively, the beam searching procedure underlines its potential over the previously used geometry-based IRS beam alignments.

C. Indoor-to-Outdoor Measurements

Scope and Setup

Fig. 15a depicts the indoor-to-outdoor scenario, wherein the connectivity of a $4\,\mathrm{m} \times 7\,\mathrm{m}$ area is considered. There are 40 UE positions in a uniform rectangular grid with 1 m spacing. The UE is mounted on a pole at a height of 1.3 m to facilitate measurements with different poses. Because of the building wall and metallic objects in the hall, most of the UE positions are situated in deep NLOS of the indoor mmWave cell, as illustrated from the bird's-eye perspective in Fig. 15b. Therefore, the mechatronic IRS is placed at a suitable outdoor position[3] in the LOS of the BS antenna at a height of 1.8 m.

[3]In advance we confirmed the suitability of this IRS placement by deploying the UE. It attains the peak connectivity of 1.97 Gbit/s DL throughput via the BS SSB beam 10. The SS-RSRP level is −77 dBm (3 dB less than for LOS UE 2 in Sec. IV-B) with an RI value of 2.0.

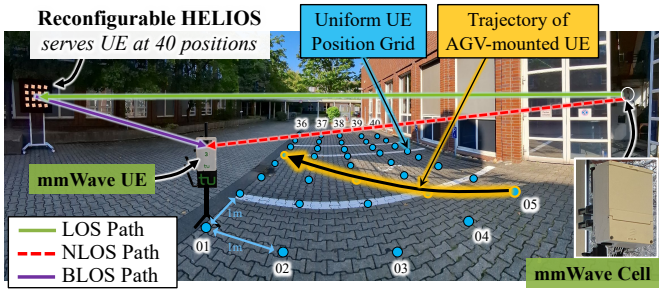

(a) Picture of outdoor UE position grid served by IRS.

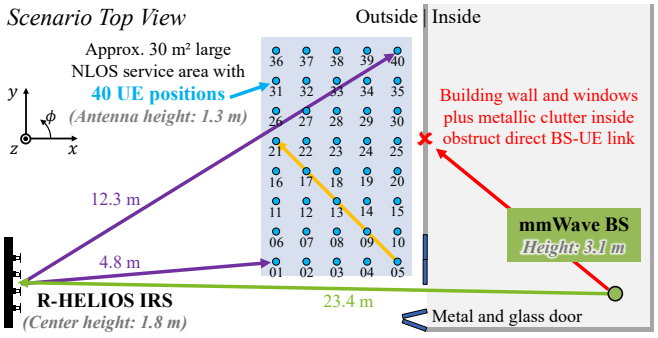

(b) Top view sketch of the indoor-to-outdoor communications scenario.

FIGURE 15. Outdoor evaluation scenario: mmWave deployment leverages R-HELIOS IRS for large-scale coverage extension and trialing of beam switching toward mobile connectivity.

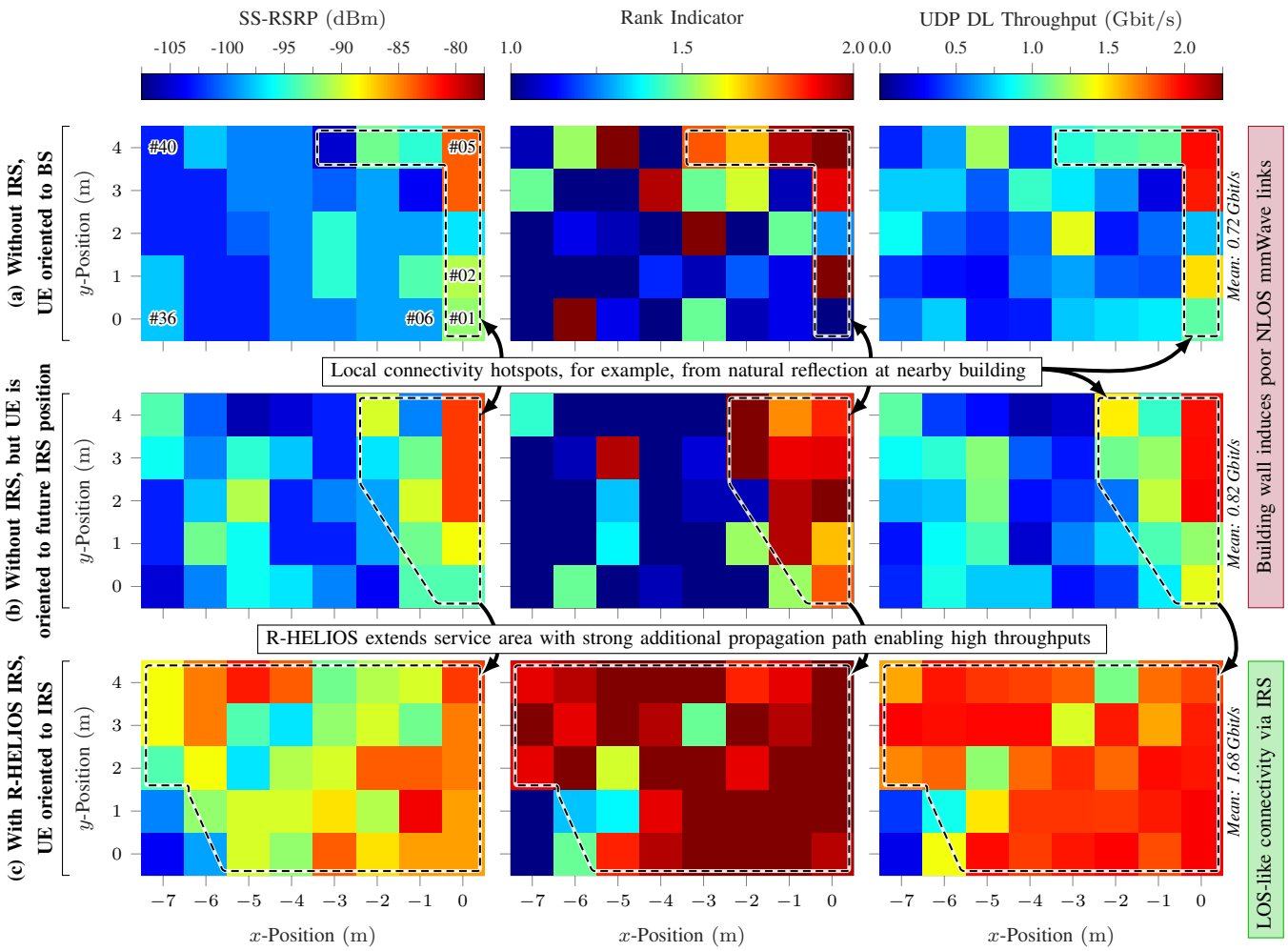

FIGURE 16. **Proposed IRS improves mmWave connectivity at 40 uniformly distributed positions by, on average, 860 Mbit/s using beamformed reflections.**

The propagation path through the open hall gate has a 3D length of 23.4 m and impinges on the reflector from direction $\phi_{in} = -1.32°, \theta_{in} = 3.23°$. The distance between the IRS and UE depends on its position and ranges from 4.8 m at position 1 to 12.3 m at position 40. The following angular space is targeted by the IRS modules to serve the service area using the individually aligned reflection beam configuration, cf. Fig. 9: $\phi_{out} \in [9.81°, 63.40°], \theta_{out} \in [-9.58°, -1.14°]$. Hence, approximately 30 % of the azimuth reflection space is serviced along with about 5 % of the elevation range. The required mechanical tilts (α_k, β_k) of R-HELIOS are calculated using UE and BS position data relative to the respective IRS modules $k = 1, \ldots, 16$. In order to thoroughly study the IRS-enabled mmWave connectivity improvements over a larger distance and area, we conduct DL measurements with and without IRS as well as with the UE oriented either toward the BS or IRS position.

Subsequently, as a brief outlook on future work, we switch to a mobile UE that is pole-mounted on a mobile robot moving in a straight line along the UE positions $\{5, 9, 13, 17, 21\}$, as illustrated by the yellow trajectory in Fig. 15a. From this point onward, we refer to the above positions in the UE grid as positions $A, B, \ldots, E$. The traversals of the automated guided vehicle (AGV) are with a constant pedestrian-like velocity and take about 10 s. We employ the reflection orchestration function to realize timed reflection beam configuration switches that are well-aligned with the UE mobility along the trajectory, cf. top right corner of Fig. 5. With this setup, we assess the impact of different IRS measures on the mobile link as a contribution to 6G IRS beam management procedures, specifically beam tracking.

Results and Discussion of Indoor-to-Outdoor Measurements

Area Coverage without and with IRS: The top and center result plots in Fig. 16 show the baseline connectivity over the study area without IRS, with the UE either oriented toward the *(a)* BS or *(b)* perspective IRS position. We observe a weak connectivity level with SS-RSRP $\leq -95\,\mathrm{dBm}$ at most positions. On the right side of the grid, i.e., near UE positions 1 to 5, the received power level is significantly higher owing to outdoor building reflection. The mean SS-RSRP values are –98.7 dBm in *(a)* and –97.1 dBm in *(b)*. A similar heatmap

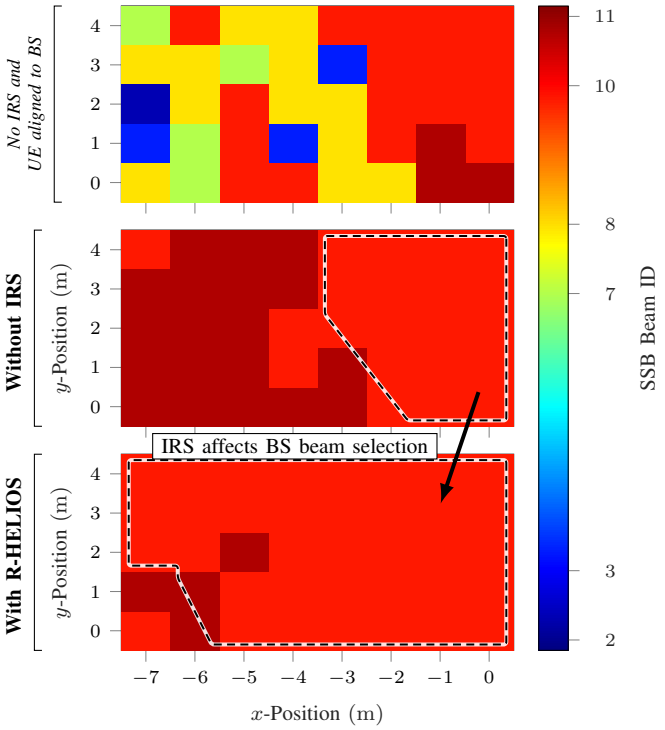

FIGURE 17. **Pencil beam utilization of mmWave cell underlines broader use of the SSB beam #10 toward the IRS to serve UEs in the service area.**

is observed for the RI metric, however, the wall reflection is exploited over a larger area in *(b)*, as the UE is mechanically oriented toward the reflecting building wall in that case. Nonetheless, the mean RI without IRS is only 1.34 and indicates that the use of two MIMO layers is prohibited at most positions owing to the wall blockage. Except for a few positions, the achievable data rate is therefore typically less than a Gigabit per second with a minimum observed data rate of about 0.1 Gbit/s given an SS-RSRP of less than −105 dBm. However, the mean DL UDP throughput is 0.72 Gbit/s in *(a)* and 0.82 Gbit/s in *(b)*.

We now introduce the R-HELIOS with the ensuing mmWave connectivity level depicted in Fig. 16c. The SS-RSRP REM on the left side differs positively from those without IRS (situated above), with numerous positions served at −90 dBm or higher. This highlights received power gains of more than 15 dB at numerous UE positions, thus corroborating the gains observed in related outdoor performance studies, e.g., [55, 101]. As expected, however, the received power level remains lower than the −77 dBm we observed at the IRS position before the measurement campaign. Furthermore, the RI attains the peak value of 2.0 at 50 % of the 40 positions, with only 7 positions having a mean RI of less than 1.75. Taken together, the two heatmaps indicate that our large IRS introduces strong and stable propagation paths for mmWave UEs. This is confirmed by the REMs in Fig. 17, which depict the BS side pencil beam utilization in the form of the SSB beam index metric. Both figures show that there is an exception in the bottom-left corner of the UE position grid, for which rather strong tilts are required. Nonetheless, the IRS increases the mean throughput by about 0.86 Gbit/s with a peak increase of 1.73 Gbit/s, cf. Fig. 16c, thereby confirming that the proposed R-HELIOS IRS successfully improves connectivity in a large NLOS service area.

Mobile BLOS Connectivity: This section finds the UE attached to an AGV to evaluate mobile mmWave connectivity in a shadowed region, see photo contained in Fig. 18. The straight trajectory from position A via B, C, D, to E (numeric UE position IDs: 5, 9, 13, 17, 21) can be seen as a yellow line in Fig. 15. The trajectory is approximately 5.7 m long ($4\sqrt{2}$ m) and traversed with a velocity of 2.04 km/h. This constitutes an angular reflection beam velocity of 4.02 °/s from positions A to E, which exceeds the narrow beamwidth of the IRS's beamformed reflection. Hence, IRS reflection reconfigurations for mmWave link maintenance are necessary. Three cases are considered in this measurement campaign wherein the UE is always mechanically oriented to the R-HELIOS position. Each test case was conducted five times from which we select the best run.

At first, no IRS is deployed, as indicated by the red line in Fig. 18. Owing to building reflection, there is good connectivity near position A, which deteriorates the longer and deeper the AGV moves into the EM-shadowed area. After moving by approximately two positions, the throughput drops by more than 1.55 Gbit/s.

Second, we introduce R-HELIOS and configure it to statically serve position C, see orange line in Fig. 18. In this case, a connectivity peak is introduced in the vicinity of position C with nearly the same magnitude as that in the static measurements, cf. green reference markers and purple

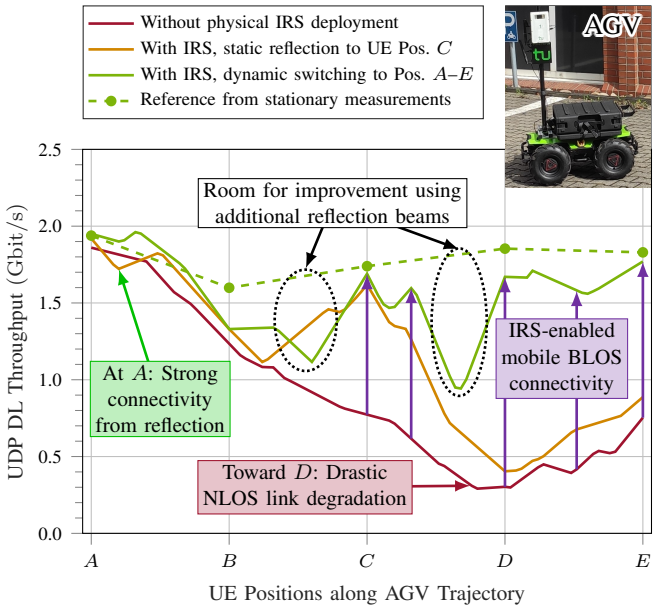

FIGURE 18. **Mobile mmWave connectivity for different R-HELIOS beam tracking schemes yielding application data rate gains beyond 1 Gbit/s. However, a higher IRS beam switching rate could be employed against occasional drops in the beyond line-of-sight connectivity.**

annotation arrows. Nonetheless, the UE is again poorly connected at positions D–E, as the UE experiences a rapid connectivity deterioration en route from C (served by static reflection beam) via D to E (both not served by IRS).

In the third and last case, the remote controller switches the R-HELIOS IRS reflection with a well-aligned timing. Consequently, the beambook reflection entry serving position A is followed by that for positions B, C, etc., thus realizing beam tracking of the mobile UE in NLOS modality. The observed performance with a dynamic reflection beam is depicted by the green line in Fig. 18, which, similar to our prior results with static UEs, dominates the performance of the previous two cases using no IRS or a narrow static IRS reflection to position C. At the five positions of interest, the downlink throughput of the static case is met in three cases (positions A, C, and E) and missed by up to approximately 270 Mbit/s at positions B and D. At position D, the throughput improvement by 1.4 Gbit/s realizes 88.7 % of the gains observed during the static measurements. Moreover, between the positions, the UE further experiences reflection misalignment-based losses, which are particularly pronounced between positions C and D with approximately 730 Mbit/s data rate reduction. Therefore, we conclude that more fine-granular beam tracking ought to be used in such scenarios in future works. The consequences of this for future 6G systems could be, for example, a significantly increased beambook size and control signaling overhead or the adoption of adaptive beamforming for the maintenance of an established IRS link.

V. CONCLUSIONS OF THE TRIALS AND OUTLOOK

This article was motivated by the expected benefits of reconfigurable IRS-assisted mmWave communications for efficient and ubiquitous 6G networks. However, our extensive examination of the state of the art in IRS technology indicated both a lack of large-scale reconfigurable mmWave reflector prototypes and insufficient experimentation in real mmWave network environments.

To address this gap, we first developed a novel mechatronically reconfigurable passive IRS prototype that extends our geometry-based static IRS HELIOS. With an effective reflecting surface area of $40\,\mathrm{cm} \times 40\,\mathrm{cm}$, it is a large-scale mmWave IRS that leverages 16 pairs of stacked servomotors for dynamic beamsteering. After laboratory validation of the power consumption and reflection alignment of the calibrated modules, the platform was complemented by an operation control center that orchestrates the IRS beam management.

Subsequently, we transferred the R-HELIOS IRS to a private cellular mmWave network environment with off-the-shelf UEs. In an industry-motivated use case wherein UEs are placed in safety cages for machinery, we used an IRS beam search to identify suitable reflection configurations. We showed that both NLOS UEs attain up to 3.6 times better connectivity with approximately 2.0 Gbit/s in DL and 0.7 Gbit/s in UL, which is similar to the reference UE placed in LOS. Moreover, we found that the IRS is sufficiently large for this deployment scenario to sustain two reflection beams with LOS-like performance, thereby increasing the cell throughput during multi-user connectivity trials by 173 %.

We further employed R-HELIOS to extend the indoor-to-outdoor connectivity at 40 uniformly distributed UE positions. The IRS successfully increases the received power level and channel rank in the considered service area by position-specific beamforming configurations, thereby realizing mean and peak DL throughput improvements of 0.9 Gbit/s and 1.7 Gbit/s, respectively. Our IRS beam tracking trial with a mobile UE demonstrated a good connectivity near the positions served by the preselected beams. However, we found that higher spatiotemporal tracking is required for a stable multi-Gbit/s performance.

Our ongoing research transfers IRSs to real-world applications. For example, robust and reliable wireless communications in the scope of modern rescue robotics shall be realized by an improved IRS beam tracking serving mobile UEs via live position estimates.

ACKNOWLEDGMENT

The authors would like to thank Mr. Marco Danger and Mr. Christian Arendt for providing access to the STING units and network companion for the mmWave measurements. We are also grateful to Dr.-Ing. Pascal Jörke and Mr. Kevin Šabanović for sharing their experience with the servomotors and 3D-printed holder/stabilization systems.

REFERENCES

[1] Ericsson AB, "Ericsson mobility report november 2024." [Online]. Available: https://www.ericsson.com/en/reports-and-papers/mobility-report/reports/november-2024 (Accessed 2025-03-03).

[2] T. S. Rappaport, R. W. Heath, R. C. Daniels, and J. N. Murdock, *Millimeter Wave Wireless Communications*, 1st ed. Pearson Prentice Hall, Sep. 2014, ISBN: 9780132172288.

[3] E. Dahlman, S. Parkvall, and J. Sköld, *5G NR: The Next Generation Wireless Access Technology*, 2nd ed. Elsevier Academic Press, Sep. 2020, ISBN: 9780128223215.

[4] 3rd Generation Partnership Project (3GPP), "TSG RAN; NR; BS radio transmission and reception (release 18)," Technical Specification (TS) 38.104, Dec. 2022, version 18.0.0.

[5] Qualcomm Inc. (2021, Jun.) Extended-range 5G world record over mmWave. [Online]. Available: https://www.qualcomm.com/news/releases/2021/06/nokia-qualcomm-and-uscellular-hit-extended-range-5g-world-record-over (Accessed 2025-03-03).

[6] Nokia Corp. (2024, Jun.) Extended range mmWave 5G speed record in Finland. [Online]. Available: https://www.nokia.com/about-us/news/releases/2023/06/26/nokia-hits-extended-range-mmwave-5g-speed-record-in-finland (Accessed 2025-03-03).

[7] T. S. Rappaport *et al.*, "Millimeter wave mobile communications for 5G cellular: It will work!" *IEEE Access*, vol. 1, pp. 335–349, May 2013, DOI: 10.1109/ACCESS.2013.2260813.

[8] S. Mohebi *et al.*, "Sectors, beams and environmental impact on the performance of commercial 5G mmWave cells: An empirical study," *IEEE Access*, vol. 10, pp. 133 309–133 323, Dec. 2022, DOI: 10.1109/ACCESS.2022.3229588.

[9] A. Narayanan *et al.*, "A comparative measurement study of commercial 5G mmWave deployments," in *Proc. IEEE INFOCOM Conf.*, May 2022, DOI: 10.1109/INFOCOM48880.2022.9796693.

[10] SK Telecom Co., Ltd., "6G white paper: 5G lesson learned, 6G key requirements, 6G network evolution, and 6G spectrum," White Paper, ICT Infra, Version 1.0, Aug. 2023. [Online]. Available: https://ee.cdnartwhere.eu/wp-content/uploads/2023/08/SKT6G-White-PaperEng-v1.0-web.pdf (Accessed 2025-03-

03).

[11] A. F. Molisch *et al.*, "Millimeter-wave channels in urban environments," in *Proc. EuCAP Conf.*, Apr. 2016, IEEE. DOI: 10.1109/EuCAP.2016.7481098.

[12] L. Possenti *et al.*, "A study on mm-Wave propagation in and around buildings," *IEEE Open J. Antennas Propag.*, vol. 4, pp. 736–747, Jul. 2023, DOI: 10.1109/OJAP.2023.3297201.

[13] M. Danger, C. Arendt, H. Schippers, S. Böcker, M. Mühleisen, P. Becker, J. B. Caro, G. Gjorgjievska, M. A. Latif, J. Ansari, N. Beckmann, N. König, R. Schmitt, and C. Wietfeld, "Performance evaluation of IRS-enhanced mmWave connectivity for 6G industrial networks," in *Proc. IEEE M&N Symp.*, Jul. 2024, DOI: 10.1109/MN60932.2024.10615534. Dataset available: https://github.com/tudo-cni/TUDo-Industrial-mmWave-Dataset. Best Paper Young Author Award.

[14] E. Theodoropoulou *et al.*, "Top challenges in 5G densification," in *Proc. IFIP AIAI Conf.*, Jun. 2021, Springer Cham. DOI: 10.1007/978-3-030-79157-5_11.

[15] Z. Li, H. Hu, J. Zhang, and J. Zhang, "Enhancing indoor mmWave wireless coverage: Small-cell densification or reconfigurable intelligent surfaces deployment?" *IEEE Wirel. Commun. Lett.*, vol. 10, no. 11, pp. 2547–2551, Aug. 2021, DOI: 10.1109/LWC.2021.3106821.

[16] M. Di Renzo, F. H. Danufane, and S. Tretyakov, "Communication models for reconfigurable intelligent surfaces: From surface electromagnetics to wireless networks optimization," *Proc. IEEE*, vol. 110, no. 9, pp. 1164–1209, Sep. 2022, DOI: 10.1109/JPROC.2022.3195536.

[17] Q. Wu, S. Zhang, B. Zheng, C. You, and R. Zhang, "Intelligent reflecting surface-aided wireless communications: A tutorial," *IEEE Trans. Commun.*, vol. 69, no. 5, pp. 3313–3351, May 2021, DOI: 10.1109/TCOMM.2021.3051897.

[18] B. Zheng, C. You, W. Mei, and R. Zhang, "A survey on channel estimation and practical passive beamforming design for intelligent reflecting surface aided wireless communications," *IEEE Commun. Surveys Tuts.*, vol. 24, no. 2, pp. 1035–1071, May 2022, DOI: 10.1109/COMST.2022.3155305.

[19] M. Rossanese, A. Garcia-Saavedra, A. E. Lutu, and X. Costa Perez, "Data-driven analysis of the cost-performance trade-off of reconfigurable intelligent surfaces in a production network," *Proc. ACM Netw.*, vol. 1, no. 12, pp. 1–20, Dec. 2023, DOI: 10.1145/3629134.

[20] R. Flamini *et al.*, "Toward a heterogeneous smart electromagnetic environment for millimeter-wave communications: An industrial viewpoint," *IEEE Trans. Antennas Propag.*, vol. 70, no. 10, pp. 8898–8910, Oct. 2022, DOI: 10.1109/TAP.2022.3151978.

[21] Rohde & Schwarz GmbH & Co. KG, "Reconfigurable intelligent surfaces: Test and measurement aspects," White Paper, Version 2.0, Nov. 2023. [Online]. Available: https://www.rohde-schwarz.com/us/solutions/wireless-communications-testing/landingpages/whitepaper-reconfigurable-intelligent-surfaces-ris-_256930.html (Accessed 2025-03-03).

[22] European Telecommunications Standards Institute (ETSI), Industry Specification Group (ISG) on RIS, "Reconfigurable Intelligent Surfaces (RIS); use cases, deployment scenarios and requirements," Group Report (GR) 001, Feb. 2025, version 1.2.1.

[23] B. Rana, S.-S. Cho, and I.-P. Hong, "Review paper on hardware of reconfigurable intelligent surfaces," *IEEE Access*, vol. 11, pp. 29 614–29 634, Mar. 2023, DOI: 10.1109/ACCESS.2023.3261547.

[24] L. F. Abanto-Leon *et al.*, "LiquiRIS: A major step towards fast beam switching in liquid crystal-based RISs," *arXiv Signal Processing (eess.SP)*, pp. 1–13, Oct. 2024, DOI: 10.48550/arXiv.2410.21506, preprint.

[25] V. Tapio, I. Hemadeh, A. Mourad, A. Shojaeifard, and M. Juntti, "Survey on reconfigurable intelligent surfaces below 10 GHz," *EURASIP J. Wirel. Commun. Netw.*, no. 1, pp. 1–18, Sep. 2021, DOI: 10.1186/s13638-021-02048-5.

[26] X. Pei *et al.*, "RIS-aided wireless communications: Prototyping, adaptive beamforming, and indoor/outdoor field trials," *IEEE Trans. Commun.*, vol. 69, no. 12, pp. 8627–8640, Dec. 2021, DOI: 10.1109/TCOMM.2021.3116151.

[27] J. Huang *et al.*, "Reconfigurable intelligent surfaces: Channel characterization and modeling," *Proc. IEEE*, vol. 110, no. 9, pp. 1290–1311, Sep. 2022, DOI: 10.1109/JPROC.2022.3186087.

[28] P. Dinh, M. Ghoshal, D. Koutsonikolas, and J. Widmer, "Demystifying resource allocation policies in operational 5G mmWave networks," in *Proc. IEEE WoWMoM Symp.*, Jun. 2022, DOI: 10.1109/WoWMoM54355.2022.00016.

[29] M. Ghoshal *et al.*, "An in-depth study of uplink performance of 5G mmWave networks," in *Proc. ACM SIGCOMM Wkshps.*, Aug. 2022, DOI: 10.1145/3538394.3546042.

[30] A. Ramírez-Arroyo *et al.*, "FR2 5G networks for industrial scenarios: Experimental characterization and beam management procedures in operational conditions," *IEEE Trans. Veh. Technol.*, vol. 73, no. 9, pp. 13 513–13 525, Sep. 2024, DOI: 10.1109/TVT.2024.3393533.

[31] J. E. Arévalo, A. E. Núñez, C. A. Azurdia, J. L. Araque, and J. I. Sandoval, "Experimental indoor coverage of a commercial mm-Wave 5G network," in *Proc. IEEE AP-S Symp. & USNC-URSI Radio Science Meeting*, Jul. 2023, DOI: 10.23919/USNC-URSI54200.2023.10289282.

[32] M. Kaudewitz, F. Schmickmann, and S. Häger. Reconfigurable HELIOS platform. [Online]. Available: https://github.com/tudo-cni/Reconfigurable_HELIOS (Accessed 2025-05-02).

[33] C. Liaskos, A. Tsioliaridou, A. Pitsillides, S. Ioannidis, and I. Akyildiz, "Using any surface to realize a new paradigm for wireless communications," *Commun. ACM*, vol. 61, no. 11, pp. 30–33, Nov. 2018, DOI: 10.1145/3192336.

[34] M. Di Renzo *et al.*, "Smart radio environments empowered by reconfigurable AI meta-surfaces: an idea whose time has come," *EURASIP J. Wirel. Commun. Netw.*, no. 129, pp. 1–20, Dec. 2019, DOI: 10.1186/s13638-019-1438-9.

[35] S. R. Hasan, S. R. Sabuj, M. Hamamura, and M. A. Hossain, "A comprehensive review on reconfigurable intelligent surface for 6G communications: Overview, deployment, control mechanism, application, challenges, and opportunities," *Wirel. Pers. Commun.*, vol. 139, no. 1, pp. 375–429, Nov. 2024, Springer Science+Business Media. DOI: 10.1007/s11277-024-11630-1.

[36] G. Oliveri, F. Zardi, L. Tosi, and A. Massa, "On the use of specular reflecting passive EM skins in NLOS wireless backhauling – performance and design guidelines," *IEEE Trans. Antennas Propag.*, vol. 72, no. 10, pp. 7893–7904, Oct. 2024, DOI: 10.1109/TAP.2024.3438940.

[37] A. Petosa *et al.*, "Characterization and enhancement of the environment for 5G millimetre-wave broadband mobile communications," in *Proc. EuCAP Conf.*, Apr. 2018, IET. DOI: 10.1049/cp.2018.0710.

[38] N. Yu *et al.*, "Light propagation with phase discontinuities: Generalized laws of reflection and refraction," *Science*, vol. 334, no. 6054, pp. 333–337, Sep. 2011, AAAS. DOI: 10.1126/science.1210713.

[39] S. Häger, K. Heimann, S. Böcker, and C. Wietfeld, "Holistic enlightening of blackspots with passive tailorable reflecting surfaces for efficient urban mmWave networks," *IEEE Access*, vol. 11, pp. 39 318–39 332, Apr. 2023, DOI: 10.1109/ACCESS.2023.3267676.

[40] F. A. Aoudia, J. Hoydis, and A. Keller. Differentiable ray tracing and radio maps [video]. [Online]. Available: https://developer.nvidia.com/blog/fast-and-differentiable-radio-maps-with-nvidia-instant-rm (Accessed 2025-03-03).

[41] D. Tagliaferri, M. Mizmizi, G. Oliveri, U. Spagnolini, and A. Massa, "Reconfigurable and static EM skins on vehicles for localization," *IEEE Trans. Wirel. Commun.*, vol. 23, no. 11, pp. 16 155–16 171, Nov. 2024, DOI: 10.1109/TWC.2024.3437778.

[42] W. Tang *et al.*, "Wireless communications with reconfigurable intelligent surface: Path loss modeling and experimental measurement," *IEEE Trans. Wirel. Commun.*, vol. 20, no. 1, pp. 421–439, Jan. 2021, DOI: 10.1109/TWC.2020.3024887.

[43] S. Meng *et al.*, "An efficient multi-beam generation method for millimeter-wave reconfigurable intelligent surface: Simulation and measurement," *IEEE Trans. Veh. Technol.*, vol. 72, no. 10, pp. 13 752–13 757, Oct. 2023, DOI: 10.1109/TVT.2023.3278459.

[44] A. Shokair *et al.*, "Real world field trial for RIS-aided commercial 5G mmWave wireless communication," in *Proc. EuCNC/6G Summit*, Jun. 2024, IEEE. DOI: 10.1109/EuCNC/6GSummit60053.2024.10597120.

[45] J. Chen, W. Wang, and J. Wang, "Opportunistic passive beamforming for RIS-assisted WiFi network: System design and experimental validation," *IEEE IoT J.*, vol. 11, no. 18, pp. 30 131–30 144, Sep. 2024, DOI: 10.1109/JIOT.2024.3411119.

[46] N. M. Tran, M. M. Amri, J. H. Park, D. I. Kim, and K. W. Choi, "Multifocus techniques for reconfigurable intelligent surface-aided

wireless power transfer: Theory to experiment," *IEEE IoT J.*, vol. 9, no. 21, pp. 21 338–21 356, Nov. 2022, DOI: 10.1109/JIOT.2022.3179691.

[47] J. S. Romero-Pena and N. Cardona, "Irregular multifocal reflector for efficient mmWave propagation in indoor enviroments," in *Proc. EuCAP Conf.*, Mar. 2020, IEEE. DOI: 10.23919/EuCAP48036.2020.9136074.

[48] M. Hwang *et al.*, "Demonstration of millimeter-wave reconfigurable intelligent surface (RIS) with built-in sensors for automatic tracking of direction-of-arrival (DOA)," *IEEE Sensors Lett.*, vol. 7, no. 8, pp. 1–4, Jul. 2023, DOI: 10.1109/LSENS.2023.3294523.

[49] K. Weinberger, S. Tewes, and A. Sezgin, "Show me the way: Real-time tracking of wireless mobile users with UWB-enabled RIS," in *Proc. ISWCS Symp.*, Jul. 2024, IEEE. DOI: 10.1109/ISWCS61526.2024.10639136.

[50] B. Xie *et al.*, "Thin film reconfigurable intelligent surface for harmonic beam steering," *IEEE Sensors Lett.*, vol. 8, no. 9, pp. 1–4, Aug. 2024, DOI: 10.1109/LSENS.2024.3438458.

[51] A. Tishchenko *et al.*, "Autonomous reconfigurable intelligent surface based on highly-efficient solar cells," in *Proc. EuCAP Conf.*, Mar. 2023, IEEE. DOI: 10.23919/EuCAP57121.2023.10133121.

[52] D. Ha *et al.*, "Passive repeater for removal of blind spot in NLOS path for 5G fixed wireless access (FWA) system," in *Proc. IEEE AP-S Symp. & USNC-URSI Radio Science Meeting*, Jul. 2017, DOI: 10.1109/APUSNCURSINRSM.2017.8073067.

[53] C-K. Wen *et al.*, "Shaping a smarter electromagnetic landscape: IAB, NCR, and RIS in 5G standard and future 6G," *IEEE Commun. Stand. Mag.*, vol. 8, no. 1, pp. 72–78, Mar. 2024, DOI: 10.1109/MCOMSTD.0008.2300036.

[54] S. Häger, S. Böcker, and C. Wietfeld, "Reflection modeling of modular passive IRS geometries," *IEEE Wirel. Commun. Lett.*, vol. 14, no. 5, pp. 1366–1370, May 2025, DOI: 10.1109/LWC.2025.3542564.

[55] D. Kitayama *et al.*, "5G radio access experiments on coverage expansion using metasurface reflector at 28 GHz," in *Proc. IEEE APMC Conf.*, Dec. 2019, DOI: 10.1109/APMC46564.2019.9038267.

[56] C. J. Vaca-Rubio *et al.*, "Assessing wireless sensing potential with large intelligent surfaces," *IEEE Open J. Commun. Soc.*, vol. 2, pp. 934–947, Apr. 2021, DOI: 10.1109/OJCOMS.2021.3073467.

[57] S. Hu, H. Wang, and M. C. Ilter, "Design of near-field beamforming for large intelligent surfaces," *IEEE Trans. Wirel. Commun.*, vol. 23, no. 1, pp. 762–774, Jan. 2024, DOI: 10.1109/TWC.2023.3281885.

[58] R. J. Williams, E. de Carvalho, and T. L. Marzetta, "A communication model for large intelligent surfaces," in *Proc. IEEE ICC Wkshps.*, Jun. 2020, DOI: 10.1109/ICCWorkshops49005.2020.9145091.

[59] M. Jung, W. Saad, Y. Jang, G. Kong, and S. Choi, "Performance analysis of large intelligent surfaces (LISs): Asymptotic data rate and channel hardening effects," *IEEE Trans. Wirel. Commun.*, vol. 19, no. 3, pp. 2052–2065, Mar. 2020, DOI: 10.1109/TWC.2019.2961990.

[60] A. Pereira, F. Rusek, M. Gomes, and R. Dinis, "Deployment strategies for large intelligent surfaces," *IEEE Access*, vol. 10, pp. 61 753–61 768, Jun. 2022, DOI: 10.1109/ACCESS.2022.3181757.

[61] K. Heimann, A. Marsch, B. Sliwa, and C. Wietfeld, "Reflecting surfaces for beyond line-of-sight coverage in millimeter wave vehicular networks," in *Proc. IEEE VNC Conf.*, Dec. 2020, DOI: 10.1109/VNC51378.2020.9318411.

[62] N. Decarli and D. Dardari, "Communication modes with large intelligent surfaces in the near field," *IEEE Access*, vol. 9, pp. 165 648–165 666, Dec. 2021, DOI: 10.1109/ACCESS.2021.3133707.

[63] Z. Cui, P. Zhang, and S. Pollin, "6G wireless communications in 7-24 GHz band: Opportunities, techniques, and challenges," *arXiv Systems and Control (eess.SY)*, pp. 1–8, Jun. 2024, DOI: 10.48550/arXiv.2310.06425, preprint. Presented at IEEE DySPAN Symp. 2025.

[64] R. Wang, Y. Yang, B. Makki, and A. Shamim, "A wideband reconfigurable intelligent surface for 5G millimeter-wave applications," *IEEE Trans. Antennas Propag.*, vol. 72, no. 3, pp. 2399–2410, Mar. 2024, DOI: 10.1109/TAP.2024.3352828.

[65] H. Matsuno *et al.*, "Development of a direction-variable liquid crystal meta-surface reflector," in *Proc. IEEE ICC Conf.*, May 2022, DOI: 10.1109/ICC45855.2022.9838358.

[66] X. Wan *et al.*, "Reconfigurable sum and difference beams based on a binary programmable metasurface," *IEEE Antennas Wireless Propag. Lett.*, vol. 20, no. 3, pp. 381–385, Mar. 2021, DOI: 10.1109/LAWP.2021.3050808.

[67] J. Jeong, J. H. Oh, S. Y. Lee, Y. Park, and S.-H. Wi, "An improved path-loss model for reconfigurable-intelligent-surface-aided wireless communications and experimental validation," *IEEE Access*, vol. 10, pp. 98 065–98 078, Sep. 2022, DOI: 10.1109/ACCESS.2022.3205117.

[68] X. Tan, Z. Sun, D. Koutsonikolas, and J. M. Jornet, "Enabling indoor mobile millimeter-wave networks based on smart reflect-arrays," in *Proc. IEEE INFOCOM Conf.*, Apr. 2018, pp. 270–278, DOI: 10.1109/INFOCOM.2018.8485924.

[69] H. Jeong, E. Park, R. Phon, and S. Lim, "Mechatronic reconfigurable intelligent-surface-driven indoor fifth-generation wireless communication," *Adv. Intell. Syst.*, vol. 4, no. 12, pp. 1–9, Dec. 2022, John Wiley & Sons, Inc. DOI: 10.1002/aisy.202200185.

[70] L. G. da Silva, L. C. Alexandre, P. Xiao, and A. Cerqueira S., "RIS development and implementation in a mm-Waves 5G-NR system toward 6G," *IEEE Wirel. Commun. Lett.*, vol. 13, no. 3, pp. 736–740, Mar. 2024, DOI: 10.1109/LWC.2023.3341301.

[71] M. Z. Chen *et al.*, "Accurate and broadband manipulations of harmonic amplitudes and phases to reach 256 QAM millimeter-wave wireless communications by time-domain digital coding metasurface," *Natl. Sci. Rev.*, vol. 9, no. 1, pp. 1–11, Jul. 2021, Oxford University Press. DOI: 10.1093/nsr/nwab134.

[72] J. Tang *et al.*, "Transmissive RIS for B5G communications: Design, prototyping, and experimental demonstrations," *IEEE Trans. Commun.*, vol. 71, no. 11, pp. 6605–6615, Nov. 2023, DOI: 10.1109/TCOMM.2023.3292477.

[73] M. Cui *et al.*, "Demo: Low-power communications based on RIS and AI for 6G," in *Proc. IEEE ICC Wkshps.*, May 2022, DOI: 10.1109/ICCWorkshops53468.2022.9915019.

[74] K. Qian, L. Yao, X. Zhang, and T. N. Ng, "MilliMirror: 3D printed reflecting surface for millimeter-wave coverage expansion," in *Proc. ACM MobiCom Conf.*, Oct. 2022, DOI: 10.1145/3495243.3517024.

[75] Orange SA, "Mobile network technology evolutions beyond 2030," White Paper, Apr. 2024. [Online]. Available: https://hellofuture.orange.com/app/uploads/2024/05/2024-Orange-white-paper-on-Mobile-Network-Technology-Evolutions-Beyond-2030.pdf (Accessed 2025-03-03).

[76] M. Giordani, M. Polese, A. Roy, D. Castor, and M. Zorzi, "A tutorial on beam management for 3GPP NR at mmWave frequencies," *IEEE Commun. Surveys Tuts.*, vol. 21, no. 1, pp. 173–196, Feb. 2019, DOI: 10.1109/COMST.2018.2869411.

[77] M. Danger, S. Häger, K. Heimann, S. Böcker, and C. Wietfeld, "Empowering 6G industrial indoor networks: Hands-on evaluation of IRS-enabled multi-user mmWave connectivity," in *Proc. EuCNC/6G Summit Conf.*, Jun. 2024, IEEE. DOI: 10.1109/EuCNC/6GSummit60053.2024.10597036.

[78] B. Kim *et al.*, "28 GHz propagation analysis for passive repeaters in NLOS channel environment," in *Proc. EuCAP Conf.*, Apr. 2015, IEEE. URL: https://ieeexplore.ieee.org/document/7228596.

[79] K. Goto, S. Suyama, T. Yamada, K. Arai, and O. Kagaya, "Experimental trials with combination of multiple transmissive metasurfaces and beamforming for mmW coverage enhancement," in *Proc. IEEE VTC-Fall Conf.*, Oct. 2023, DOI: 10.1109/VTC2023-Fall60731.2023.10333724.

[80] K. Heimann, S. Häger, and C. Wietfeld, "Demo abstract: Experimental 6G research platform for digital twin-enabled beam management," in *Proc. ACM MobiWac Symp.*, Oct. 2023, DOI: 10.1145/3616390.3618282. Demo video: https://tiny.cc/HeliosDemonstrator.

[81] G. C. Trichopoulos *et al.*, "Design and evaluation of reconfigurable intelligent surfaces in real-world environment," *IEEE Open J. Commun. Soc.*, vol. 3, pp. 462–474, Mar. 2022, DOI: 10.1109/OJCOMS.2022.3158310.

[82] J. Sang *et al.*, "Coverage enhancement by deploying RIS in 5G commercial mobile networks: Field trials," *IEEE Wirel. Commun.*, vol. 31, no. 1, pp. 172–180, Feb. 2024, DOI: 10.1109/MWC.011.2200356.

[83] A. S. Shekhawat, B. G. Kashyap, R. W. R. Torres, F. Shan, and G. C. Trichopoulos, "A millimeter-wave single-bit reconfigurable intelligent surface with high-resolution beam-steering and suppressed quantization lobe," *IEEE Open J. Antennas Propag.*, vol. 6, no. 1, pp. 311–325, Feb. 2025, DOI: 10.1109/OJAP.2024.3506453.

[84] E. Martinez-de-Rioja *et al.*, "Dual-coverage electromagnetic skin with independent shaped beams for sub-THz 6G communications," *IEEE Access*, vol. 12, pp. 134 624–134 634, Sep. 2024, DOI: 10.1109/ACCESS.2024.3461608.

[85] E. Martinez-de Rioja, A. Arboleya, F. R. Varela, and C. Fontá, "Dual-band electromagnetic skin with independent reflection performance at 28 GHz and 39 GHz for 5G millimeter-wave communications," *IEEE Antennas Wireless Propag. Lett.*, vol. 23, no. 10, pp. 3138–3142, Oct. 2024, DOI: 10.1109/LAWP.2024.3427772.

[86] Y. Kawamoto *et al.*, "Near-field behaviors of intelligent reflecting surface: Experimental measurements at 60GHz," in *Proc. IEEE APWCS Symp.*, Aug. 2024, DOI: 10.1109/APWCS61586.2024.10679298.

[87] M. M. Amri, N. M. Tran, and K. W. Choi, "Reconfigurable intelligent surface-aided wireless communications: Adaptive beamforming and experimental validations," *IEEE Access*, vol. 9, pp. 147 442–147 457, Oct. 2021, DOI: 10.1109/ACCESS.2021.3124319.

[88] Y. Yuan *et al.*, "Field trial of reconfigurable intelligent surface with statistics-based optimization for 5G commercial networks," *IEEE Wirel. Commun.*, vol. 31, no. 3, pp. 390–397, Jun. 2024, DOI: 10.1109/MWC.006.2300166.

[89] T. Mazloum *et al.*, "Indoor channel characterization using transmitting and reflecting RIS at mmWaves," *IEEE Trans. Antennas Propag.*, vol. 73, no. 4, pp. 2026–3037, Apr. 2025, DOI: 10.1109/TAP.2024.3499335.

[90] Y. Li, *Intelligent Reflecting Surfaces in Wireless Communication Systems*. KIT Scientific Publishing, Feb. 2024, ISBN: 9783731513346.

[91] M. Ouyang *et al.*, "Computer vision-aided reconfigurable intelligent surface-based beam tracking: Prototyping and experimental results," *IEEE Trans. Wirel. Commun.*, vol. 22, no. 12, pp. 8681–8693, Dec. 2023, DOI: 10.1109/TWC.2023.3264752.

[92] A. Schott, A. Ichkov, P. Mähönen, and L. Simić, "Measurement validation of ray-tracing propagation modeling for mm-Wave networking studies: How detailed is detailed enough?" in *Proc. EuCAP Conf.*, Mar. 2023, IEEE. DOI: 10.23919/EuCAP57121.2023.10132941.

[93] L. Dai *et al.*, "Reconfigurable intelligent surface-based wireless communications: Antenna design, prototyping, and experimental results," *IEEE Access*, vol. 8, pp. 45 913–45 923, Mar. 2020, DOI: 10.1109/ACCESS.2020.2977772.

[94] V. Arun and H. Balakrishnan, "RFocus: Beamforming using thousands of passive antennas," in *Proc. USENIX NSDI Symp.*, Feb. 2020, URL: https://www.usenix.org/system/files/nsdi20-paper-arun.pdf.

[95] J. Sang *et al.*, "Multi-scenario broadband channel measurement and modeling for sub-6 GHz RIS-assisted wireless communication systems," *IEEE Trans. Wirel. Commun.*, vol. 23, no. 6, pp. 6312–6329, Jun. 2024, DOI: 10.1109/TWC.2023.3330977.

[96] Z. Zhang *et al.*, "Macromodeling of reconfigurable intelligent surface based on microwave network theory," *IEEE Trans. Antennas Propag.*, vol. 70, no. 10, pp. 8707–8717, Oct. 2022, DOI: 10.1109/TAP.2022.3187645.

[97] J. Rains, A. Tukmanov, Q. Abbasi, and M. Imran, "RIS-enhanced MIMO channels in urban environments: Experimental insights," in *Proc. EuCAP Conf.*, Mar. 2024, IEEE. DOI: 10.23919/EuCAP60739.2024.10501311.

[98] A. Araghi *et al.*, "Reconfigurable intelligent surface (RIS) in the sub-6 GHz band: Design, implementation, and real-world demonstration," *IEEE Access*, vol. 10, pp. 2646–2655, Jan. 2022, DOI: 10.1109/ACCESS.2022.3140278.

[99] F. Yi, K. W. Cho, Y. Xie, and K. Jamieson, "WaveFlex: A smart surface for private 5G CBRS networks," *Proc. ACM Netw.*, vol. 2, no. 37, pp. 1–21, Nov. 2024, DOI: 10.1145/3696394.

[100] A. Hu, K. Konno, Q. Chen, and T. Takahashi, "A highly efficient 1-bit reflectarray antenna using electromagnet-controlled elements," *IEEE Trans. Antennas Propag.*, vol. 72, no. 1, pp. 506–517, Jan. 2024, DOI: 10.1109/TAP.2023.3324457.

[101] R. Liu, J. Dou, P. Li, J. Wu, and Y. Cui, "Simulation and field trial results of reconfigurable intelligent surfaces in 5G networks," *IEEE Access*, vol. 10, pp. 122 786–122 795, Nov. 2022, DOI: 10.1109/ACCESS.2022.3223447.

[102] D. Vabichevich, A. Belov, and A. Sayanskiy, "Suppression of quantization lobes in 1-bit reconfigurable intelligent surfaces," *IEEE Antennas Wireless Propag. Lett.*, vol. 22, no. 12, pp. 2808–2811, Dec. 2023, DOI: 10.1109/LAWP.2023.3299198.

[103] S. Kayraklik, I. Yildirim, Y. Gevez, E. Basar, and A. Görçin, "Indoor coverage enhancement for RIS-assisted communication systems: Practical measurements and efficient grouping," in *Proc. IEEE ICC Conf.*, Jun. 2023, pp. 485–490, DOI: 10.1109/ICC45041.2023.10278759.

[104] T. Chen *et al.*, "Reconfigurable intelligent surface (RIS)-assisted wireless communications with a virtual reality (VR) case study," in *Proc. IET 6G Conf.*, Jun. 2024, DOI: 10.1049/icp.2024.2235.

[105] French Ministry of Armed Forces. Flat, intelligent and reconfigurable satcom antenna. [Online]. Available: https://archives.defense.gouv.fr/aid/actualites/l-antenne-satcom-plate-intelligente-et-reconfigurable.html (Accessed 2025-03-03).

[106] M. Rossanese *et al.*, "Open experimental measurements of sub-6GHz reconfigurable intelligent surfaces," *IEEE Internet Comput.*, vol. 28, no. 2, pp. 19–28, Mar. 2024, DOI: 10.1109/MIC.2024.3376772.

[107] S. Tewes, M. Heinrichs, K. Weinberger, R. Kronberger, and A. Sezgin, "A comprehensive dataset of RIS-based channel measurements in the 5GHz band," in *Proc. IEEE VTC-Spring Conf.*, Jun. 2023, DOI: 10.1109/VTC2023-Spring57618.2023.10200973.

[108] L. Wu *et al.*, "A wideband amplifying reconfigurable intelligent surface," *IEEE Trans. Antennas Propag.*, vol. 70, no. 11, pp. 10 623–10 631, Nov. 2022, DOI: 10.1109/TAP.2022.3187137.

[109] B. Beiranvand and R. Mirzavand, "Enhancing wireless applications through reconfigurable electro-mechanical reflectarray antenna design for beam steering," *Sci. Rep.*, vol. 14, no. 30140, pp. 1–18, Dec. 2024, Springer Nature. DOI: 10.1038/s41598-024-81421-y.

[110] Y. Wang, W. Wang, Y. Wu, and W. Fan, "RIS codebook-based beamsteering validation and field trials," *IET Electron. Lett.*, vol. 60, no. 14, pp. 1–5, Jul. 2024, DOI: 10.1049/ell2.13273.

[111] J. Zhang *et al.*, "Cascaded channel modeling and experimental validation for RIS assisted communication system," *arXiv Signal Processing (eess.SP)*, pp. 1–6, Dec. 2024, DOI: 10.48550/arXiv.2412.07356, preprint.

[112] Q. Xu *et al.*, "Mechanically reprogrammable Pancharatnam–Berry metasurface for microwaves," *Adv. Photonics*, vol. 4, no. 1, pp. 1–11, Feb. 2022, SPIE. DOI: 10.1117/1.AP.4.1.016002.

[113] S. M. A. Momeni Hasan Abadi, J. H. Booske, and N. Behdad, "MAcro-Electro-Mechanical Systems (MÆMS) based concept for microwave beam steering in reflectarray antennas," *J. Appl. Phys.*, vol. 120, no. 5, pp. 1–8, Aug. 2016, AIP Publishing LLC. DOI: 10.1063/1.4960352.

[114] G. Oliveri, F. Zardi, and A. Massa, "On the improvement of the performance of inexpensive electromagnetic skins by means of an inverse source design approach," *IEEE Transactions on Antennas and Propagation*, pp. 1–12, Jan. 2025, DOI: 10.1109/TAP.2025.3529203, early access.

[115] W-Y. Chung *et al.*, "WiRiS: Transformer for RIS-assisted device-free sensing for joint people counting and localization using Wi-Fi CSI," in *Proc. IEEE PIMRC Symp.*, Sep. 2023, DOI: 10.1109/PIMRC56721.2023.10293762.

[116] Y-C. Lin *et al.*, "Effects of large angle of incidence in offset-fed reflectarray antennas," in *Proc. IEEE AP-S Symp. & USNC-URSI Radio Science Meeting*, Jul. 2019, DOI: 10.1109/APUSNCURSINRSM.2019.8888331.

[117] X. Cao, Q. Chen, T. Tanaka, M. Kozai, and H. Minami, "A 1-bit time-modulated reflectarray for reconfigurable-intelligent-surface applications," *IEEE Trans. Antennas Propag.*, vol. 71, no. 3, pp. 2396–2408, Mar. 2023, DOI: 10.1109/TAP.2022.3233659.

[118] J. P. S. Wong, M. Selvanayagam, and G. V. Eleftheriades, "Polarization considerations for scalar Huygens metasurfaces and characterization for 2-D refraction," *IEEE Trans. Microw. Theory Techn.*, vol. 63, no. 3, pp. 913–924, Mar. 2015, DOI: 10.1109/TMTT.2015.2392931.

[119] K. MacDonell, D. Kundu, C. Andersen, L. M. Rufail, and S. Gupta, "Mechatronic shape-shifting reflector platform for dynamic beam-steering," in *Proc. URSI GASS Symp.*, Aug. 2023, DOI: 10.46620/URSIGASS.2023.1388.AEJN6716.

[120] K. MacDonell, D. Kundu, C. Andersen, L. M. Rufail, and S. Gupta, "A mechatronic shape-shifting reflector system with true independent reflection magnitude and phase control for dynamic beamforming," *TechRxiv*, pp. 1–11, Aug. 2023, DOI: 10.36227/techrxiv.23735958, preprint.

[121] Y. Zhao *et al.*, "2-bit RIS prototyping enhancing rapid-response space-time wavefront manipulation for wireless communication: Experimental studies," *IEEE Open J. Commun. Soc.*, vol. 5, pp. 4885–4901, Aug. 2024, DOI: 10.1109/OJCOMS.2024.3439558.

[122] H. Yu *et al.*, "Quad-polarization reconfigurable reflectarray with independent beam-scanning and polarization switching capabilities," *IEEE Trans. Antennas Propag.*, vol. 71, no. 9, pp. 7285–7298, Sep. 2023, DOI: 10.1109/TAP.2023.3291460.

[123] M. K. T. Al-Nuaimi, W. G. Whittow, G.-L. Huang, R.-S. Chen, and S.-W. Wong, "Wideband radar-cross-section reduction using parabolic phased metasurfaces," *IEEE Antennas Wireless Propag. Lett.*, vol. 22, no. 7, pp. 1547–1551, Jul. 2023, DOI: 10.1109/LAWP.2023.3250453.

[124] K. W. Cho, M. H. Mazaheri, J. Gummeson, O. Abari, and K. Jamieson, "mmWall: A steerable, transflective metamaterial surface for NextG mmWave networks," in *Proc. USENIX NSDI Symp.*, Apr. 2023, URL: https://www.usenix.org/system/files/nsdi23-cho-kun-woo.pdf.

[125] K. W. Cho, P. Maddala, I. Seskar, and K. Jamieson, "Demo: Metasurface-enabled NextG mmWave for roadside networking," in *Proc. ACM MobiCom Conf.*, Nov. 2024, DOI: 10.1145/3636534.3698839.

[126] P. Mei, S. Zhang, and G. F. Pedersen, "A low-cost, high-efficiency and full-metal reflectarray antenna with mechanically 2-D beam-steerable capabilities for 5G applications," *IEEE Trans. Antennas Propag.*, vol. 68, no. 10, pp. 6997–7006, Oct. 2020, DOI: 10.1109/TAP.2020.2993077.

[127] J. Ethier, R. Chaharmir, J. Shaker, and K. Hettak, "Electromagnetic engineered surface gratings at 5G bands using printed electronics," in *Proc. IFETC Conf.*, Aug. 2018, IEEE. DOI: 10.1109/IFETC.2018.8583977.

[128] A. Petosa, "Engineering the 5G environment," in *Proc. IEEE 5G World Forum (5GWF)*, Jul. 2018, DOI: 10.1109/5GWF.2018.8516930.

[129] Y. Li *et al.*, "Path loss modeling for the RIS-assisted channel in a corridor scenario in mmWave bands," in *Proc. IEEE Globecom Wkshps.*, Dec. 2022, DOI: 10.1109/GCWkshps56602.2022.10008687.

[130] S. K. R. Vuyyuru, L. Hao, M. Rupp, S. A. Tretyakov, and R. Valkonen, "Modeling RIS from electromagnetic principles to communication systems – part I: Synthesis and characterization of a scalable anomalous reflector," *IEEE Trans. Antennas Propag.*, vol. 73, no. 3, pp. 1743–1755, Mar. 2025, DOI: 10.1109/TAP.2024.3520416.

[131] L. Hao *et al.*, "Modeling RIS from electromagnetic principles to communication systems – part II: System-level simulation, ray tracing, and measurement," *IEEE Trans. Antennas Propag.*, vol. 73, no. 3, pp. 1756–1767, Mar. 2025, DOI: 10.1109/TAP.2025.3533902.

[132] ZTE Corp. The first dynamic RIS 2.0 field trial. [Online]. Available: https://www.zte.com.cn/global/solutions_latest/5g-advanced/ris.html (Accessed 2025-03-03).

[133] D. Kwon *et al.*, "Field evaluation of reconfigurable intelligent surface with varying surface size," in *Proc. IEEE AP-S Symp. & USNC-URSI Radio Science Meeting*, Jul. 2023, DOI: 10.1109/USNC-URSI52151.2023.10238136.

[134] H. Yang *et al.*, "Beyond limitations of 5G with RIS: Field trial in a commercial network, recent advances, and future directions," *IEEE Commun. Mag.*, vol. 62, no. 10, pp. 132–138, Oct. 2024, DOI: 10.1109/MCOM.024.2300440.

[135] TMY Technology Inc., "XRifle: Reflector ES series," Datasheet, May 2023. [Online]. Available: https://tmytek.com/products/components/xrifle (Accessed 2025-03-03).

[136] M. Mehlhose. Developing 5G mmWave deployment with XRifle reflector [video]. [Online]. Available: https://www.youtube.com/watch?v=yASTVabvEU4 (Accessed 2025-03-03).

[137] W. Khawaja, O. Ozdemir, Y. Yapici, F. Erden, and I. Güvenc, "Coverage enhancement for NLOS mmWave links using passive reflectors," *IEEE Open J. Commun. Soc.*, vol. 1, pp. 263–281, Jan. 2020, DOI: 10.1109/OJCOMS.2020.2969751.

[138] TMY Technology Inc., "XRifle dynamic RIS specification: Dynamic 28," Datasheet, Apr. 2024. [Online]. Available: https://www.tmytek.com/products/components/xrifle-dynamic-ris (Accessed 2025-03-03).

[139] W. Chen and F. Gerhardes. Dynamic RIS technology revealed - field deployment performance and evaluation [video]. [Online]. Available: https://www.youtube.com/watch?v=g2r9wtzAKUg (Accessed 2025-03-03).

[140] S. Häger, M. Danger, K. Heimann, Y. Gümüs, S. Böcker, and C. Wietfeld, "Custom design and experimental evaluation of passive reflectors for mmWave private networks," in *Proc. IEEE LANMAN Symp.*, Jul. 2024, DOI: 10.1109/LANMAN61958.2024.10621891. Best Paper Award.

[141] A. S. Shekhawat, B. G. Kashyap, P. C. Theofanopoulos, A. P. S. Sengar, and G. C. Trichopoulos, "A compact unit-cell design for mmWave reconfigurable intelligent surfaces," in *Proc. USNC-URSI National Radio Science Meeting (USNC-URSI NRSM)*, Jan. 2022, IEEE. DOI: 10.23919/USNC-URSINRSM57467.2022.9881473.

[142] A. S. Shekhawat, B. G. Kashyap, B. Tjahjadi, and G. C. Trichopoulos, "Beamforming characterization of a mmWave single-bit reflective metasurface," in *Proc. IEEE AP-S Symp. & USNC-URSI Radio Science Meeting*, Jul. 2022, DOI: 10.1109/AP-S/USNC-URSI47032.2022.9886912.

[143] J.-B. Gros, V. Popov, M. A. Odit, V. Lenets, and G. Lerosey, "A reconfigurable intelligent surface at mmWave based on a binary phase tunable metasurface," *IEEE Open J. Commun. Soc.*, vol. 2, pp. 1055–1064, May 2021, DOI: 10.1109/OJCOMS.2021.3076271.

[144] V. Popov *et al.*, "Experimental demonstration of a mmWave passive access point extender based on a binary reconfigurable intelligent surface," *Front. Comms. Net.*, vol. 2, no. 733891, pp. 1–8, Oct. 2021, Frontiers Media SA. DOI: 10.3389/frcmn.2021.733891.

[145] Tsinghua University. Low-power communications based on RIS and AI for 6G [video]. [Online]. Available: https://oa.ee.tsinghua.edu.cn/dailinglong/research/research.html (Accessed 2025-03-03).

[146] A. Berto, F. F. Manzillo, and G. Valerio, "Design and characterization of a transmitting and reflecting metasurface at 30 GHz," in *Proc. EuMC Conf.*, Sep. 2024, IEEE. DOI: 10.23919/EuMC61614.2024.10732122.

[147] A. Massaccesi *et al.*, "3D-printed wideband reflectarray antennas with mechanical beam-steering," *Int. J. Microw. Wirel. Technol.*, vol. 16, no. 1, p. 21–29, May 2023, Cambridge University Press. DOI: 10.1017/S1759078723000776.

[148] Y. Ren *et al.*, "On deployment position of RIS in wireless communication systems: Analysis and experimental results," *IEEE Wirel. Commun. Lett.*, vol. 12, no. 10, pp. 1756–1760, Oct. 2023, DOI: 10.1109/LWC.2023.3292125.

[149] J. Wang *et al.*, "Reconfigurable intelligent surface: Power consumption modeling and practical measurement validation," *IEEE Trans. Commun.*, vol. 72, no. 9, pp. 5720–5734, Sep. 2024, DOI: 10.1109/TCOMM.2024.3382332.

[150] T. Ohto, K. Yoshikawa, H. Matsuno, and T. Nagao, "Reconfigurable intelligent surface for millimeter-wave mobile communication system: Development and coverage evaluation," in *Proc. AM-FPD Wkshps.*, Jul. 2024, IEEE. DOI: 10.1109/ICC42927.2021.9500510.

[151] J. S. Romero-Pena and N. Cardona, "Diffuse modular honeycomb passive reflector for efficient mmWave propagation in indoor environments," in *Proc. EuCNC/6G Summit*, Jun. 2022, IEEE. DOI: 10.1109/EuCNC/6GSummit54941.2022.9815699.

[152] T. J. Cui, R. Y. Wu, W. Wu, C. B. Shi, and Y. B. Li, "Large-scale transmission-type multifunctional anisotropic coding metasurfaces in millimeter-wave frequencies," *J. Phys. D: Appl. Phys.*, vol. 50, no. 40, pp. 1–9, Sep. 2017, IOP Publishing. DOI: 10.1088/1361-6463/aa85bd.

[153] H. Kamoda, T. Iwasaki, J. Tsumochi, T. Kuki, and O. Hashimoto, "60-GHz electronically reconfigurable large reflectarray using single-bit phase shifters," *IEEE Trans. Antennas Propag.*, vol. 59, no. 7, pp. 2524–2531, Jul. 2011, DOI: 10.1109/TAP.2011.2152338.

[154] A. P. Ganesh *et al.*, "Propagation measurements and coverage analysis for mmWave and sub-THz frequency bands with transparent reflectors," in *Proc. IEEE VTC-Spring Conf.*, Jun. 2023, DOI: 10.1109/VTC2023-Spring57618.2023.10200244.

[155] M. K. T. Al-Nuaimi, Y. He, and W. Hong, "Design of 1-bit coding engineered reflectors for EM-wave shaping and RCS modifications," *IEEE Access*, vol. 6, pp. 75 422–75 428, Nov. 2018, DOI: 10.1109/ACCESS.2018.2883721.

[156] M. K. T. Al-Nuaimi and W. G. Whittow, "Design of QR-coded metasurfaces for RCS reduction at mmWave," *IEEE Access*, vol. 10, pp. 66 267–66 272, Jun. 2022, DOI: 10.1109/ACCESS.2022.3182103.

[157] M. K. Taher Al-Nuaimi, W. G. Whittow, G.-L. Huang, and R.-S. Chen, "Cusp phased metasurfaces for wideband RCS reduction under broad angles of incidence," *IEEE Open J. Antennas Propag.*, vol. 5, no. 4, pp. 913–921, Aug. 2024, DOI: 10.1109/OJAP.2023.3342712.

[158] N. A. Abbasi *et al.*, "Ultra-wideband double directional channel measurements for THz communications in urban environments," in *Proc. IEEE ICC Conf.*, Jun. 2021, DOI: 10.1109/ICC42927.2021.9500510.

[159] X. Liu *et al.*, "Terahertz beam steering using a MEMS-based reflectarray configured by a genetic algorithm," *IEEE Access*, vol. 10, pp. 84 458–84 472, Aug. 2022, DOI: 10.1109/ACCESS.2022.3197202.

[160] R. Wiebusch, P. Jörke, and C. Wietfeld, "Experimental 5G platform for managing mixed-critical traffic using network slicing in concentrated solar power plants," in *Proc. IEEE SmartGridComm Conf.*, Sep. 2024, DOI: 10.1109/SmartGridComm60555.2024.10738060.
[161] Lynxmotion Inc. Pan and tilt standard scale servo. [Online]. Available: https://wiki.lynxmotion.com/info/wiki/lynxmotion/view/ses-v1/ses-v1-robots/ses-v1-misc-mechanical/pan-tilt-standard (Accessed 2025-03-03).
[162] 3M Corp., "EMI copper foil shielding tape 1181," Datasheet, Jun. 2021. [Online]. Available: https://multimedia.3m.com/mws/media/37370O/3m-emi-copper-foil-shielding-tape-1181-data-sheet-78-8127-9953-0-b.pdf (Accessed 2025-03-03).
[163] ARC Technologies LLC, "ML-10052 (ML-77 series)," Technical Data Sheet, Jan. 2019. [Online]. Available: https://www.cdiweb.com/datasheets/arc/ml10052reve.pdf (Accessed 2025-03-03).
[164] Raspberry Pi Ltd., "Pico W: An RP2040-based microcontroller board with wireless," Datasheet, Oct. 2024. [Online]. Available: https://datasheets.raspberrypi.com/picow/pico-w-datasheet.pdf (Accessed 2025-03-03).
[165] NXP Semiconductors N.V. PCA9685 controller. [Online]. Available: https://www.nxp.com/products/PCA9685 (Accessed 2025-03-03).
[166] The Qt Company Ltd. Qt for python documentation. [Online]. Available: https://doc.qt.io/qtforpython-6/ (Accessed 2025-03-03).
[167] Conrad Electronic SE, "Digital angle gauge TO-6547356," Operating Instructions, 2020. [Online]. Available: https://asset.conrad.com/media10/add/160267/c1/-/gl/002182452ML00/bedienungsanleitung-2340313-toolcraft-to-6547356-digitaler-winkelmesser-kalibriert-iso-360.pdf (Accessed 2025-03-03).
[168] Ansys Inc. High frequency simulation software (HFSS). [Online]. Available: www.ansys.com/hfss (Accessed 2025-03-03).
[169] Keysight Technologies, Inc. N6705C DC power analyzer. [Online]. Available: https://www.keysight.com/us/en/product/N6705C (Accessed 2025-03-03).
[170] A. Narayanan *et al.*, "A variegated look at 5G in the wild: performance, power, and QoE implications," in *Proc. ACM SIGCOMM Conf.*, Aug. 2021, DOI: 10.1145/3452296.3472923.
[171] S. K. Saha *et al.*, "A detailed look into power consumption of commodity 60 GHz devices," in *Proc. IEEE WoWMoM Symp.*, Jun. 2017, DOI: 10.1109/WoWMoM.2017.7974282.
[172] Gaustech. RIS. [Online]. Available: https://gaustech.org/products/ris/gs-ris265.html (Accessed 2025-03-03).
[173] YTTEK Technology Corp. Y.RIS - liquid crystal RIS. [Online]. Available: https://yttek.com/solution/y-ris (Accessed 2025-03-03).
[174] C. Arendt, S. Böcker, C. Bektas, and C. Wietfeld, "Better safe than sorry: Distributed testbed for performance evaluation of private networks," in *Proc. IEEE Future Networks World Forum (FNWF)*, Oct. 2022, DOI: 10.1109/FNWF55208.2022.00041.
[175] R. Deban, H. Boutayeb, K. Wu, and J. Conan, "Deterministic approach for spatial diversity analysis of radar systems using near-field radar cross section of a metallic plate," *IEEE Trans. Antennas Propag.*, vol. 58, no. 3, pp. 908–916, Mar. 2010, DOI: 10.1109/TAP.2009.2039328.

BIOGRAPHIES

SIMON HÄGER (Graduate Student Member, IEEE) earned his M.Sc. degree in Communications Engineering from RWTH Aachen University, Aachen, Germany, in 2020, and his B.Sc. degree in Electrical Engineering from Paderborn University, Paderborn, Germany, in 2018. During the winter of 2019–2020, he completed an internship at Ericsson Research, located in Herzogenrath, Germany. He is currently pursuing the Dr.-Ing. degree at TU Dortmund University, Dortmund, Germany, with a focus on mobile cellular millimeter-wave communications leveraging custom-tailored passive reflectors to enhance connectivity efficiently. For instance, this research was honored with the Best Paper Award at the IEEE LANMAN Symposium 2024. His work at the Communication Networks Institute (CNI) also investigates beam management procedures and native channel-based sensing services for 6G mmWave networks.

MARCEL KAUDEWITZ received the M.Sc. degree from TU Dortmund University, Dortmund, Germany, in 2024. He is currently employed as a Research Assistant at the Communication Networks Institute (CNI), Faculty of Electrical Engineering and Information Technology, TU Dortmund University. His research focuses on mechatronically reconfigurable reflecting surfaces for improved millimeter-wave connectivity in future wireless 6G communication networks.

FLORIAN SCHMICKMANN (Member, IEEE) received the M.Sc. degree from TU Dortmund University, Dortmund, Germany, in 2022. He is currently employed as a Research Assistant at the Communication Networks Institute (CNI), Faculty of Electrical Engineering and Information Technology, TU Dortmund University. His main research interests are wireless localization systems, using technologies such as ultra-wideband mesh networking and inertial sensing. He has experience with designing wireless mobile sensor platforms, embedded systems, as well as application programming.

STEFAN BÖCKER received his Dipl.-Ing. degree from TU Dortmund University, Dortmund, Germany, in 2013. He started as a Research Assistant at the Communication Networks Institute (CNI), Faculty of Electrical Engineering and Information Technology, TU Dortmund University. In 2016 he took over as the institute's Head of the Research Group for 5G networks before being appointed Chief Engineer in 2021, where he is currently responsible for the coordination of third-party funded research activities. His main research interests are scalability in unlicensed frequency domains, 5G networks with a focus on mMTC, as well as operation of private networks in licensed domains with a special interest in industrial IoT environments.

CHRISTIAN WIETFELD (Senior Member, IEEE) received the Dr.-Ing. and Dipl.-Ing. degrees from RWTH Aachen University, Aachen, Germany. He is currently a Full Professor and the Head of the Communication Networks Institute at TU Dortmund University, Dortmund, Germany. For more than 30 years, he has been a Coordinator of and a Contributor to large-scale research projects on Internet-based mobile communication systems within both academia and industry at RWTH Aachen (1992–1997), Siemens AG (1997–2005), and TU Dortmund (2005 to date). His current research interests include the design and performance evaluation of 5G and 6G communication networks for cyber-physical systems in energy, transport, robotics, and emergency response. Prof. Wietfeld is the author of more than 400 peer-reviewed papers and holds several patents. He has been a Co-Founder of the IEEE Global Communications Conference Workshop on Wireless Networking for Unmanned Autonomous Vehicles and is a Member of the Technical Editor Board of the IEEE Wireless Communication Magazine. In addition to more than 15 IEEE Best Paper Awards, he was the recipient of the ITU-T Outstanding Contribution Award for his work on the standardization of next-generation mobile network architectures.